Electronic Supplementary Information (ESI)

A dual-emitting Cu_6-Cu_2-Cu_6 cluster as a self-calibrated, wide-range luminescent molecular thermometer

Jun-Hao Wang, Mian Li, Ji Zheng, Xiao-Chun Huang and Dan Li**

Department of Chemistry and Key Laboratory for Preparation and Application of Ordered Structural Materials of Guangdong Province, Shantou University, Guangdong 515063, P. R. China. E-mail: xchuang@stu.edu.cn; dli@stu.edu.cn

Table of Contents

Experimental Section

Materials and physical measurements:

The ligand 3,5-bis((3,5-dimethyl-1*H*-pyrazol-4-yl)methyl)-2,6-dimethylpyridine (H_2**L**) was synthesized via a procedure similar to literatures reported by others and us.[1,2,3] Other reagents and solvents were commercially available and used as received. Elemental analysis (C, H, N) was performed using a Vario EL III CHNS elemental analyzer. Thermogravimetric (TG) analysis was performed on a TA Instruments Q50 Thermogravimetric Analyzer under nitrogen flow of (40 mL·min^{-1}) at a typical heating rate of 10 °C·min^{-1}. Powder X-ray diffraction (PXRD) experiments were performed on a D8 Advance X-ray diffractometer. UV-vis spectra were measured with a Bio-Logic MOS-450/AF-CD Spectrometer. Infrared spectra (KBr pellet) were recorded on a Nicolet Avatar 360 FTIR spectrometer in the range of 4000-400 cm^{-1} (abbreviations: w = weak, m = medium, b = broad, s = strong, vs = very strong).

Steady-state luminescence spectra were carried out with a PTI QuantaMaster Model QM-TM scanning spectrofluorometer. The emission spectra were corrected for the detector response, respectively. Lifetime data were acquired using phosphorescence subsystem add-ons to the PTI instrument. The pulsed excitation source was generated using the 337.1 nm line of the N_2 laser pumping a freshly prepared 1×10^{-2} M solution of the continuum laser dye, R-590, in methanol, the output of which was appropriately tuned and frequency doubled to attain the excitation wavelengths needed based on the luminescence excitation spectra for each compound. Cooling in temperature-dependent measurements for the crystals was achieved using the Janis Research Model VPF-100 System with a liquid nitrogen tank. The lifetime decays were all fitted by the ExpDec1 function on Origin 9.0. Microcrystalline samples were used for all photoluminescence measurements. For all photophysical measurements of complex **2**, the desolvated samples (i.e. **2'**) were used in order to exclude the influence of solvents to the spectra. The desolvation of **2** to **2'** can be done by treating the samples under vacuum at 220 °C for 24 hours. The single crystal of **2'** can be measured and solved (see below). All instrument parameters such as excitation/emission slit and scanning speed were fixed in order to ensure the reliability of the luminescence intensity differences when performing varied-temperature phosphorescence spectrum test for each sample.

[1] S. Monmoton, H. Lefebvre, F. Costa-Torro, A. Fradet, *Macromol. Chem. Phys.* 2008, **209**, 2382.
[2] G.-F. Gao, M. Li, S.-Z. Zhan, Z. Lv, G.-h. Chen, D. Li, *Chem. Eur. J.* 2011, **17**, 4113.
[3] J.-H. Wang, M. Li, D. Li, *Chem. Sci.* 2013, **4**, 1793.

Synthesis

Synthesis of (2,6-dimethylpyridine-3,5-diyl)dimethanol (M1)

A solution of diethyl 2,6-dimethylpyridine-3,5-dicarboxylate (13.57 g, 0.054 mol) in diethyl ether (170.0 mL) was added dropwise under vigorous stirring to a suspension of $LiAlH_4$ (6.85 g; 0.18 mol) in diethyl ether (240.0 mL) under a nitrogen stream. After refluxing for 30 min and cooling down to room temperature, 30.0 mL of water was slowly added in order to hydrolyze $LiAlH_4$ excess. The white pasty precipitate was filtered, suspended in 100 mL methanol and heated to reflux for 6 h. The suspension was filtered at room temperature. Evaporation of the filtrate yielded M1 as a white solid (7.8 g; 86.4 %). The product was used directly for next reaction without any purification.

Synthesis of 3,5-bis(chloromethyl)-2,6-dimethylpyridine (M2)

Excess thionyl chloride (50ml) was added dropwise to a suspension of M1 (5.02g, 0.04mol) in anhydrous CCl_4 (50ml). After refluxing for 8 hours and cooling down to room temperature, the solvent and excessive $SOCl_2$ was evaporated. The product was purified through column chromatography (SiO_2) with Petroleum ether (b.p. 60-90 ^oC)/dichloromethane (6/1) as eluent, yielded M2 as a white solid (6.52g, 80.28 %). ^{1}H-NMR (400 MHz, CDCl3)，δ 8.24 (d, J = 3.7 Hz, 1H), 4.66 (d, J = 4.3 Hz, 4H), 3.08 (d, J = 4.5 Hz, 6H).

Synthesis of 3,5-bis((3,5-dimethyl-1*H*-pyrazol-4-yl)methyl)-2,6-dimethylpyridine (H$_2$L)

Sodium acetylacetonate (2.45 g, 0.02 mol) was added to a stirred, refluxing t-butyl alcohol (80 mL). After 5 min, M2 (2.03 g, 0.01 mol) was added during a 10-min period. 30 min after the addition, 0.5 g of KI and 0.2 g of 15-crown-5 were added. The reaction mixture was stirred and heated at reflux temperature for about 5 hours. After three-fourths of the solvent was distilled, the solid residue was washed thoroughly with water and extracted with dichloromethane. The extracts were dried over anhydrous Na_2SO_4 and the solvent was distilled. The residual oil was dissolved in 60 mL ethanol, and excess hydrazine hydrate was added to the solution. The solution was stirred and heated under refluxing temperature for 5 hours. After the solution was concentrated, large amount of water was added. The resultant white solid was filtered off, washed with water and dried (2.35 g, yield ca. 72.8%). ^{1}H-NMR (400 MHz, MeOD) δ 6.67 (s, 1H), 3.62 (d, J = 5.8 Hz, 4H), 2.47 (d, J = 6.6 Hz, 6H), 1.95 (d, J = 23.2 Hz, 12H).

Synthesis of 1

A mixture of H_2**L** (6.5 mg, 0.02 mmol), Cu_2O (2.8 mg, 0.02 mmol), hexane (2 mL) and acetonitrile (0.5

mL) was sealed in a Pyrex tube and heated in an oven at 180 ºC for 72 hours and slowly cooled to room temperature at a rate of 5 ºC·h^{-1}. Colorless plate crystals were obtained. Bulk samples were prepared through a reported procedure with modifications.[4] A 100 mL, two-necked, round-bottomed flask equipped with a magnetic stirrer was connected to a nitrogen line. The flask was purged thoroughly with nitrogen and charged with H_2**L** (0.969 g, 3 mmol) and acetone (40.0 mL). $[Cu(CH_3CN)_4][BF_4]$ (1.89 g, 6 mmol) was added while stirring. After the solution became clear, degassed triethylamine (1.5 mL) was added to the mixture over a period of 1 min. The product precipitated as a white solid. The resulting suspension was stirred for 1 h and then aqueous ammonium (25 %) (2 ml) was added. The resulting suspension was stirred under refluxing for another 10 hours. The product was filtered, washed with acetone (50.0 mL) and hexane (20.0 mL) and dried under reduced pressure. Anal. Calcd for $C_{57}H_{69}Cu_6N_{15}$: C 50.88, H 5.17, N 15.61 %, Found: C 50.65, H 5.19, N 15.51 %. IR data (KBr, cm^{-1}): 2901 s, 2724 w, 2287 w, 1567 m, 1507 s, 1442 s, 1371 m, 1342 m, 1306 m, 1212 s, 1147 s, 1023 m, 988 w, 952 m, 881 w, 787 s, 722 m.

Synthesis of 2

A mixture of **1** (134.5 mg, 0.1 mmol), CuI (152.4 mg, 0.8 mmol), and ethanol (2 ml) was sealed in a Pyrex tube and heated in an oven at 180 ºC for 72 hours and slowly cooled to room temperature at a rate of 5 ºC·h^{-1}. Colorless pillared crystals were obtained. (yield: 95 % based on **1**). Anal. Calcd for $C_{57}H_{69}Cu_7N_{15}I$: C 44.57, H 4.53, N 13.68 %, Found: C 44.69, H 4.69, N 13.56 % (After evacuation under vacuum at 160 ^{o}C for 10 hours). IR data (KBr, cm^{-1}): 3492 m, 2901 s, 2724 w, 2281 w, 1567 m, 1507 s, 1442 s, 1377 m, 1348 m, 1306 m, 1218 s, 1147 s, 1029 m, 988 w, 952 m, 876 w, 787 s, 722 m.

Synthesis of 3

This complex has been reported in 1980s.[5,6] In this paper, **3** was prepared through a different method. 2,6-lutidine (1 ml) was added to a suspension of CuI (381mg, 2mmol) in dichloromethane (20 ml). After stirring for 30 minutes at room temperature, the suspension was filtered. Slow evaporation of the filtrate afforded colourless block crystals. (yield: 51 % based on ligand). Anal. Calcd for $C_{14}H_{18}Cu_2I_2N_2$: C 28.25, H 3.05, N 4.71 %, Found: C 28.31, H 3.19, N 4.66 %. IR data (KBr, cm^{-1}): 2370 w, 1602 m, 1578 m, 1466 s, 1377 m, 1159 m, 1100 m, 1029 m, 781 s, 721 w.

[4] H. V. R. Dias, H. V. K. Diyabalanage, M. G. Eldabaja, O. Elbjeirami, M. A. Rawashdeh-Omary, M. A. Omary, *J. Am. Chem. Soc.* 2005, **127**, 7489.
[5] J. A. Campbell, C. L. Raston, A. H. White, *Aust. J. Chem.* 1977, **30**, 1937.
[6] P. C. Healy, J. D. Kildea, B. W. Skelton, A. H. White, *Aust. J. Chem.* 1989, **42**, 115.

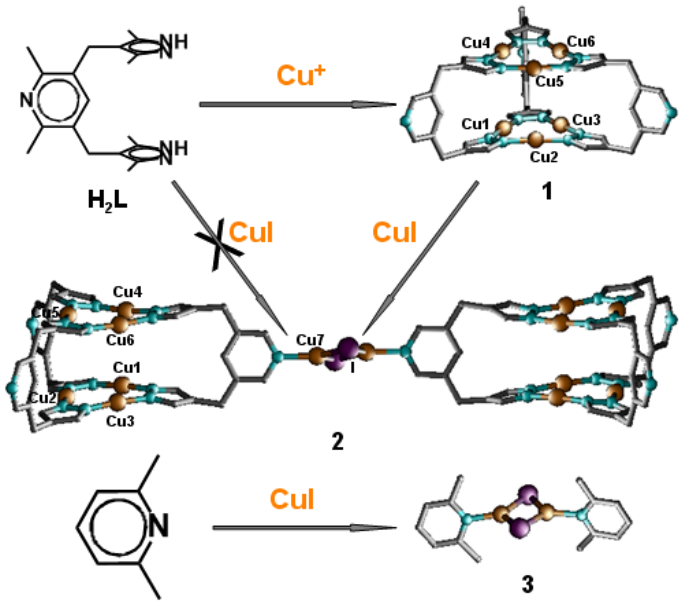

Scheme S1: Synthetic routes for compounds **1**, **2** and **3**.

Crystal Data Section

Single crystal data collection was performed on an Oxford Diffraction Gemini E (Enhance Mo X-Ray source, Kα, λ = 0.71073 Å (for **1** and **3**) and Enhance Cu X-Ray source, Kα, λ = 1.5418 Å (for **2**)) equipped with a graphite monochromator and ATLAS CCD detector (CrysAlis CCD, Oxford Diffraction Ltd) at room temperature (298 K) and under nitrogen stream (100 K, for **2** only). The single crystal of the desolvated **2'** can be measured and solved at room temperature (298 K). The data was processed using CrysAlis RED, Oxford Diffraction Ltd. Structure were solved by direct methods (SHELXTL-97) and refined on F^2 using full-matrix last-squares (SHELXTL-97).[7] All non-hydrogen atoms were refined with anisotropic thermal parameters, and all hydrogen atoms were included in calculated positions and refined with isotropic thermal parameters riding on those of the parent atoms. The treatment for the guest molecules in **2** involved the use of the SQUEEZE program of PLATON.[8] Parameters for data collection and refinement of all complexes are summarized in **Table S1**. Selected bond lengths and angles for all complexes are given in **Table S2**.

[7] G. M. Sheldrick, *Acta Crystallogra. A* 2008, **64**, 112.
[8] A. Spek, *J. Appl. Crystallogr.* 2003, **36**, 7.

Table S1. Summary of the Crystal Data and Structure Refinement Parameters

Parameters	**1**	**2 (298K)**	**2 (100K)**	**2'**	**3**
CCDC Nos.	949368	949369	949370	983600	949371
Formula	$C_{57}H_{69}Cu_6N_{15}$	$C_{57}H_{69}Cu_7N_{15}I$	$C_{57}H_{69}Cu_7N_{15}I$	$C_{57}H_{69}Cu_7N_{15}I$	$C_{14}H_{18}Cu_2I_2N_2$
M_r	1345.51	1535.95	1535.95	1535.95	595.18
Temp (*K*)	298	298	100	298	298
Space group	*P*-1	*P*-1	*P*-1	*P*-1	$P2_1/c$
a (Å)	9.300(2)	9.1825(3)	9.0947(6)	9.0869(3)	16.350(3)
b (Å)	15.907(4)	16.4791(7)	16.4229(16)	16.4643(6)	7.8394(15)
c (Å)	20.499(5)	23.3979(11)	23.0642(18)	23.4304(8)	15.389(3)
α (deg)	90.581(5)	102.410(4)	102.321(8)	102.936(3)	90
β (deg)	92.286(5)	99.703(4)	99.053(6)	100.450(3)	110.453(3)
γ (deg)	90.567(6)	99.900(3)	100.587(7)	99.938(3)	90
V(Å^3)	3029.8(14)	3327.7(2)	3238.2(5)	3275.59(19)	1848.2(6)
Z	2	2	2	2	4
D_{calcd}(g cm^{-3})	1.475	1.533	1.575	1.557	2.139
μ (mm^{-1})	2.117	6.416	2.778	6.518	5.634
Reflcns collcd	21697	21474	23282	23126	12491
Unique reflcns	10534	12166	11390	12933	3233
R_{int}	0.0719	0.0416	0.0275	0.0248	0.0334
$R1[I>2\sigma(I)]^a$	0.0625	0.0527	0.0466	0.0337	0.0464
$wR2[I>2\sigma(I)]^a$	0.1049	0.1623	0.1674	0.0974	0.1058
*R*1(all data)	0.1662	0.0824	0.0603	0.0440	0.0594
*wR*2(all data)	0.1475	0.1834	0.1828	0.1050	0.1202
GOOF	0.998	1.014	1.067	1.022	1.137

^{a} $R_1=\sum(||F_0|-|F_c||)/\sum|F_0|$; $wR_2=[\sum_w(F_0^2-F_c^2)^2/\sum w(F_0^2)^2]^{1/2}$

Table S2. Selected Bond Lengths (Å) and Bond Angles (°)

1			
Cu(1)-N(2)	1.852(6)	Cu(5)-N(9)	1.861(6)
Cu(1)-N(13)	1.855(6)	Cu(6)-N(10)	1.843(6)
Cu(2)-N(7)	1.832(6)	Cu(6)-N(14)	1.847(6)
Cu(2)-N(3)	1.845(6)	N(2)-Cu(1)-N(13)	177.6(3)
Cu(3)-N(8)	1.845(6)	N(7)-Cu(2)-N(3)	175.6(3)
Cu(3)-N(12)	1.855(6)	N(8)-Cu(3)-N(12)	176.7(3)
Cu(4)-N(4)	1.838(6)	N(4)-Cu(4)-N(15)	179.4(3)
Cu(4)-N(15)	1.864(6)	N(5)-Cu(5)-N(9)	175.1(3)
Cu(5)-N(5)	1.845(6)	N(10)-Cu(6)-N(14)	176.3(3)
2/298K			
Cu(1)-N(13)	1.853(5)	I(1)-Cu(7)#1	2.5644(10)
Cu(1)-N(2)	1.857(5)	I(1)-Cu(7)	2.5763(11)
Cu(2)-N(7)	1.849(6)	Cu(7)-Cu(7)#1	2.5543(15)
Cu(2)-N(3)	1.857(6)	N(13)-Cu(1)-N(2)	174.5(3)
Cu(3)-N(8)	1.841(5)	N(7)-Cu(2)-N(3)	177.9(3)
Cu(3)-N(12)	1.845(5)	N(8)-Cu(3)-N(12)	175.6(3)
Cu(4)-N(15)	1.858(5)	N(15)-Cu(4)-N(4)	174.4(3)
Cu(4)-N(4)	1.860(5)	N(5)-Cu(5)-N(9)	177.6(3)
Cu(5)-N(5)	1.847(6)	N(14)-Cu(6)-N(10)	174.7(3)
Cu(5)-N(9)	1.860(5)	N(11)-Cu(7)-I(1)#1	122.76(14)
Cu(6)-N(14)	1.841(5)	N(11)-Cu(7)-I(1)	116.65(14)
Cu(6)-N(10)	1.848(5)	I(1)#1-Cu(7)-I(1)	120.41(3)
Cu(7)-N(11)	2.005(4)	Cu(7)#1-I(1)-Cu(7)	59.59(3)
Symmetry codes: #1 -x+3,-y+1,-z+1			

2/100K			
Cu(1)-N(13)	1.847(5)	I(1)-Cu(7)#1	2.5762(8)
Cu(1)-N(4)	1.857(5)	I(1)-Cu(7)	2.5787(9)
Cu(2)-N(12)	1.849(5)	Cu(7)-Cu(7)#1	2.5451(13)
Cu(2)-N(8)	1.859(5)	N(13)-Cu(1)-N(4)	175.1(2)
Cu(3)-N(5)	1.847(5)	N(12)-Cu(2)-N(8)	173.7(2)
Cu(3)-N(9)	1.853(5)	N(5)-Cu(3)-N(9)	177.4(2)
Cu(4)-N(15)	1.839(5)	N(15)-Cu(4)-N(6)	174.3(2)
Cu(4)-N(6)	1.841(5)	N(14)-Cu(5)-N(10)	173.5(2)
Cu(5)-N(14)	1.851(5)	N(11)-Cu(6)-N(7)	177.4(2)
Cu(5)-N(10)	1.860(5)	N(2)-Cu(7)-I(1)#1	122.78(14)
Cu(6)-N(11)	1.850(5)	N(2)-Cu(7)-I(1)	116.07(14)
Cu(6)-N(7)	1.863(5)	I(1)#1-Cu(7)-I(1)	120.83(3)
Cu(7)-N(2)	2.006(4)	Cu(7)#1-I(1)-Cu(7)	59.17(3)
Symmetry codes: #1 -x,-y+2,-z			
2'			
I(1)-Cu(7)	2.5735(5)	Cu(2)-N(6)	1.848(3)
I(1)-Cu(7)#1	2.5602(5)	Cu(1)-N(12)	1.856(3)
Cu(4)-N(14)	1.849(3)	Cu(1)-N(2)	1.855(3)
Cu(4)-N(4)	1.849(2)	N(13)-Cu(6)-N(9)	177.74(14)
Cu(7)-Cu(7)#1	2.5933(8)	N(1)-Cu(2)-N(6)	174.11(14)
Cu(7)-N(5)	2.010(2)	N(2)-Cu(1)-N(12)	175.19(14)
Cu(5)-N(3)	1.849(2)	N(4)-Cu(4)-N(14)	174.18(13)
Cu(5)-N(8)	1.855(3)	I(1)#1-Cu(7)-I(1)	119.318(16)
Cu(3)-N(7)	1.852(3)	N(5)-Cu(7)-I(1)#1	124.62(7)
Cu(3)-N(11)	1.855(3)	N(5)-Cu(7)-I(1)	115.55(7)
Cu(6)-N(13)	1.848(3)	N(5)-Cu(7)-Cu(7)#1	171.42(8)

Cu(6)-N(9)	1.851(3)	N(3)-Cu(5)-N(8)	176.77(14)
Cu(2)-N(1)	1.842(3)	N(7)-Cu(3)-N(1)#1	177.34(15)
Symmetry codes: #1 –x, -y, 1-z			
3			
I(1)-Cu(1)	2.5731(11)	Cu(1)-I(1)-Cu(2)	59.98(3)
I(1)-Cu(2)	2.5737(12)	Cu(2)-I(2)-Cu(1)	60.80(3)
I(2)-Cu(2)	2.5354(11)	N(1)-Cu(1)-I(2)	121.91(15)
I(2)-Cu(1)	2.5482(11)	N(1)-Cu(1)-I(1)	118.97(15)
Cu(1)-N(1)	1.980(5)	I(2)-Cu(1)-I(1)	119.11(4)
Cu(1)-Cu(2)	2.5725(12)	N(2)-Cu(2)-I(2)	122.48(16)
Cu(2)-N(2)	1.990(5)	N(2)-Cu(2)-I(1)	117.93(16)
		I(2)-Cu(2)-I(1)	119.57(4)

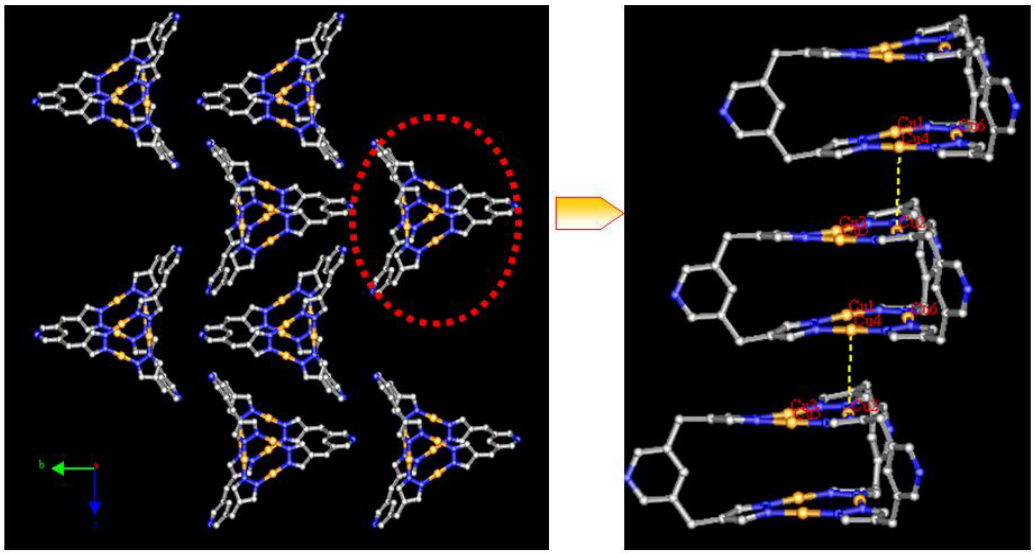

(a) **(b)**

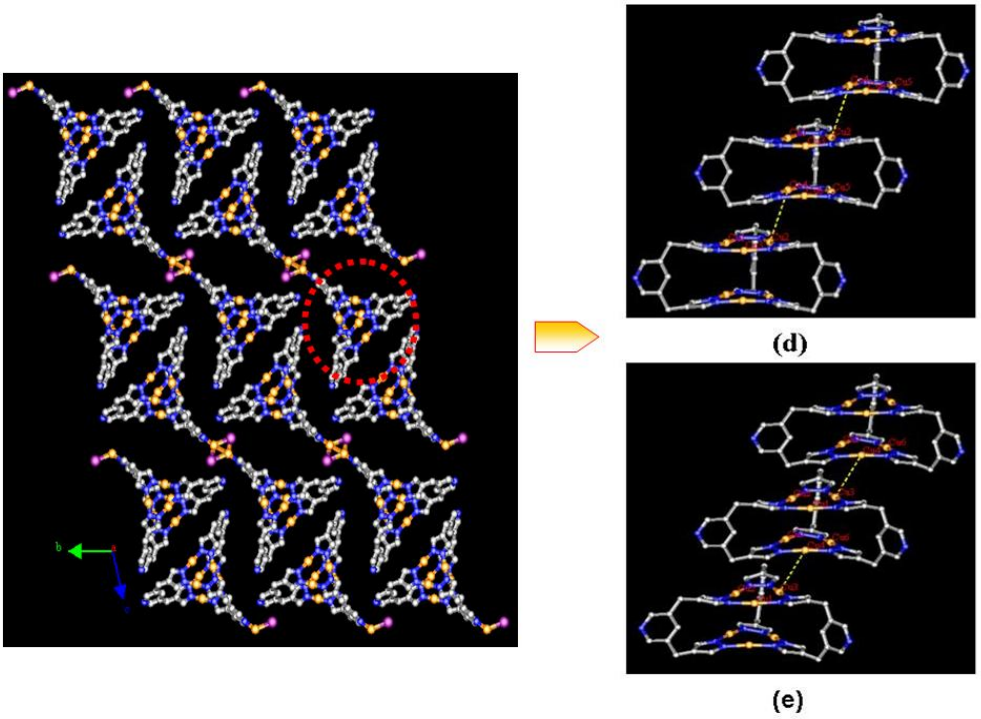

(c)

(d)

(e)

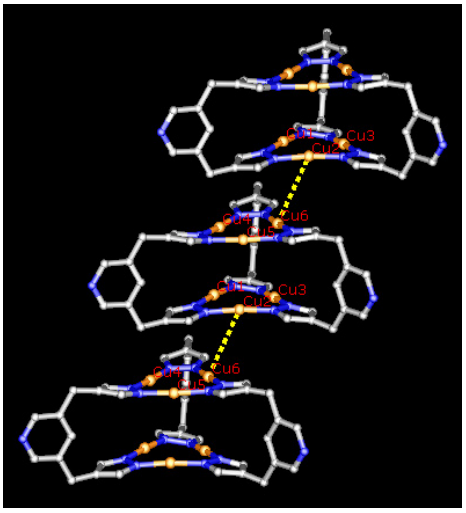

(f)

Fig. S1: (a) Packing diagrams of the complex **1** from *a* direction; (b) Detailed packing diagrams of the cage in **1,** besides the intertrimeric Cu^{I}-Cu^{I} interaction with distance of 4.040, 4.190, and 4.370 Å, intercage Cu^{I}-Cu^{I} interaction with distance of 4.1317 Å was also observed; (c) Packing diagrams of the complex **2** from *a* direction; (d) Detailed packing diagrams of the cage in **2** at room temperature, intertrimeric Cu^{I}-Cu^{I} distance:3.8289, 3.9782, 4.2147 Å; intercage Cu^{I}-Cu^{I} distance: 4.2563 Å; (e) Detailed packing diagrams of the cage in **2** at 100 K, intertrimeric Cu^{I}-Cu^{I} distance:3.7388, 3.8821, 4.1812 Å; intercage Cu^{I}-Cu^{I} distance: 4.2049 Å (f) Detailed packing diagrams of the cage in **2'** (after heating **2** for 24 hours at 220 °C under vacuum), intertrimeric Cu^{I}-Cu^{I} distance:3.888, 4.035, 4.258 Å; intercage Cu^{I}-Cu^{I} distance: 4.2440 Å.

Physical Measurement Section

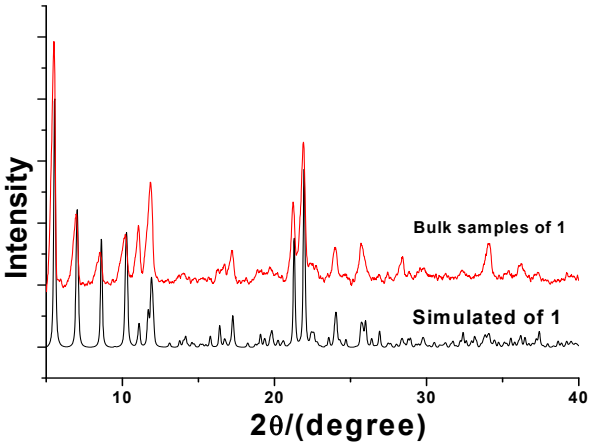

(a)

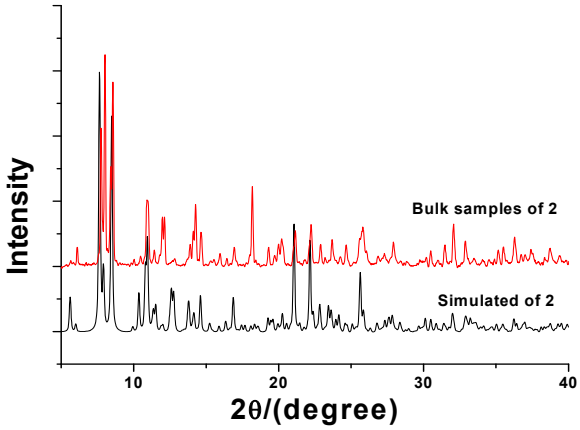

(b)

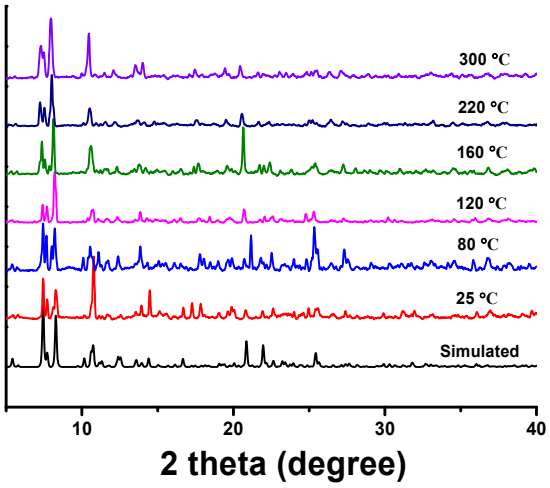

(c)

Fig. S2: Comparison of experimental PXRD for bulk samples with simulated patterns from single-crystal X-ray data: (a) complex **1**; (b) complex **2** and (c) complex **2** at different temperatures.

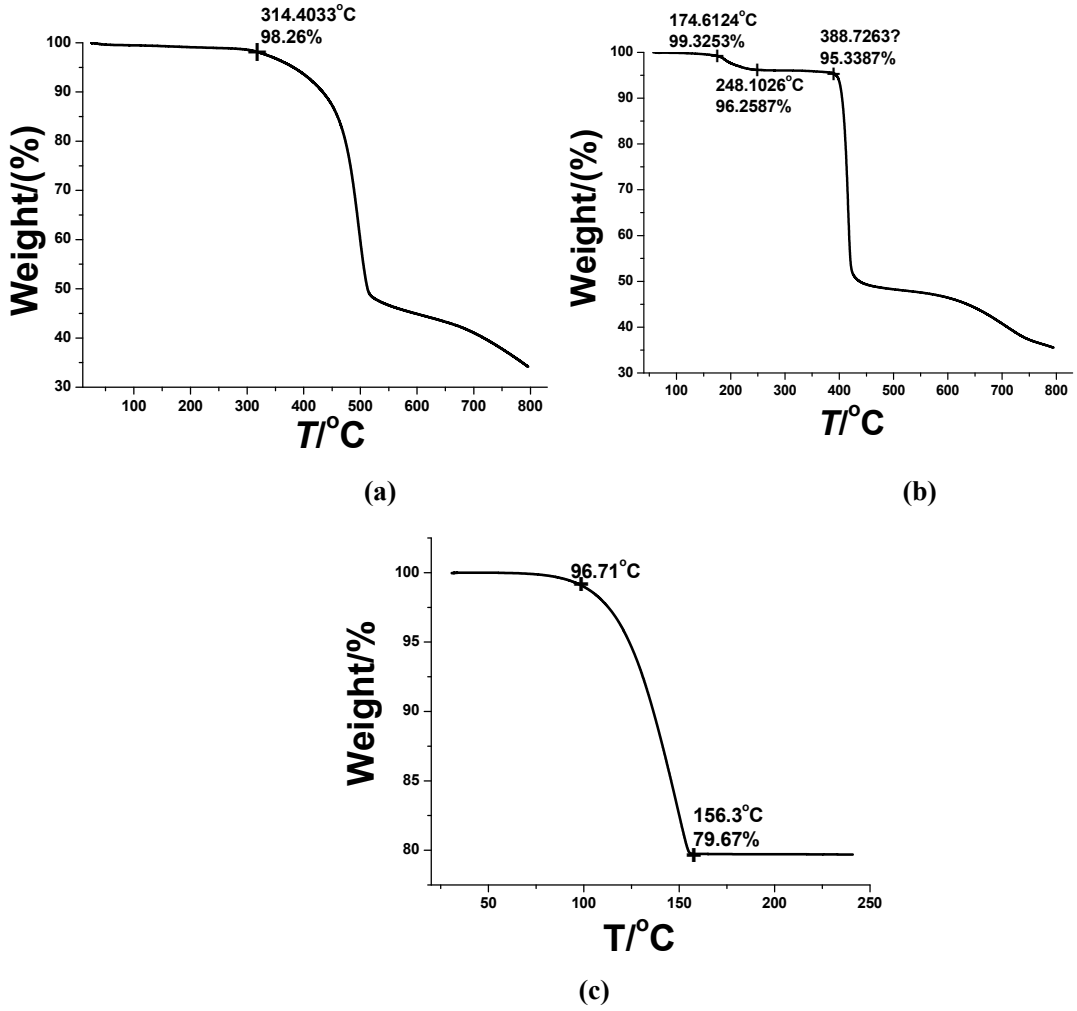

Fig. S3: TG analysis of curves of (a) **1;** (b) **2**; and (c) **3**. The mass loss of ca. 3.06 % from 174.6 °C to 248.1 °C is related to the loss of guest ethanol solvates (calculated value 2.91 %). We found the binary compound **2** showed better thermal stability than its components **1** and **3**.

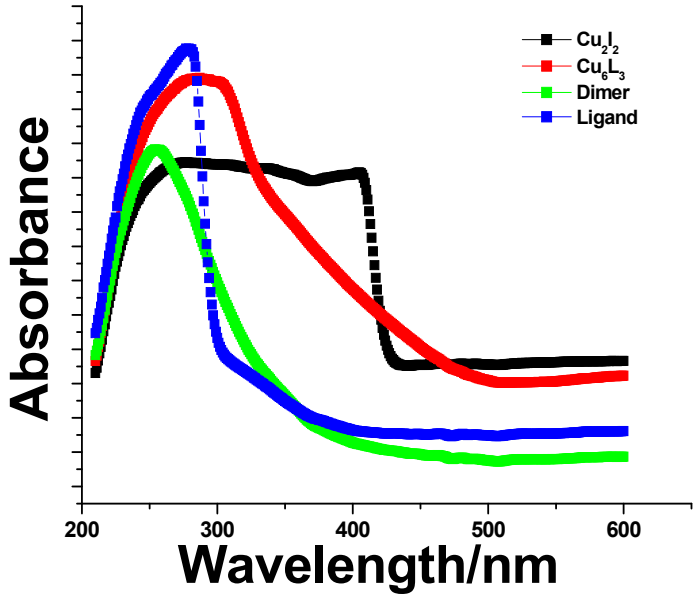

Fig. S4: UV-vis spectra of **1** (Cu_6L_3), **2** (Dimer), **3** (Cu_2I_2) and the ligand in the solid states.

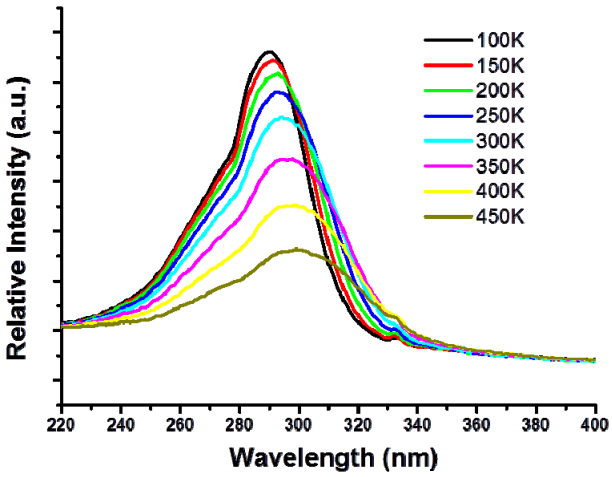

Fig. S5: Solid-state excitation spectra of **1** monitored by 740 nm under various temperatures. The dependence of excitation spectra on temperature is similar to previous reports (see ref. 9a in the main text), which is attributed to the shortening of Cu^{I}-Cu^{I} contacts and multiple excited states at low temperatures.

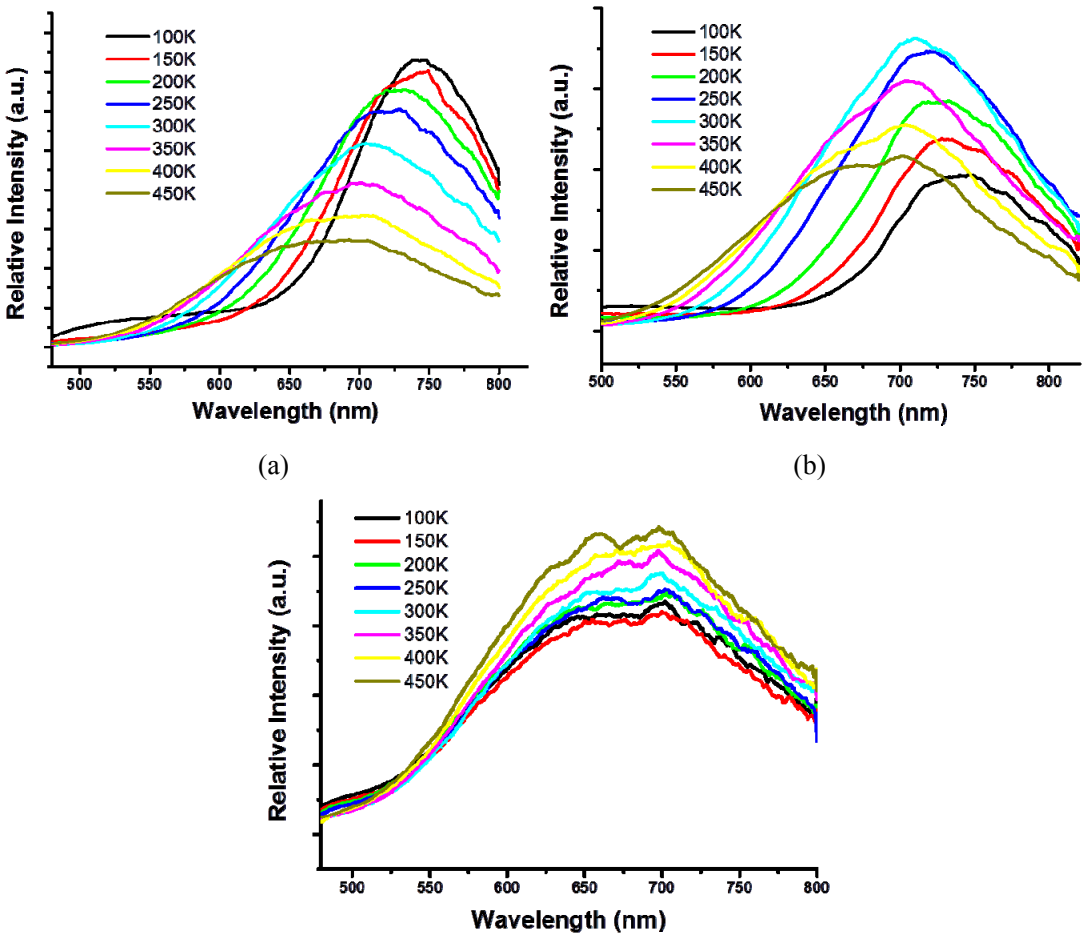

Fig. S6: (a) Solid-state emission spectra of **1** upon excited at 290 nm (a), 310 nm (b) and 340 nm (c) upon varying temperature from 100 to 450 K (excitation spectra given in Fig. S5).

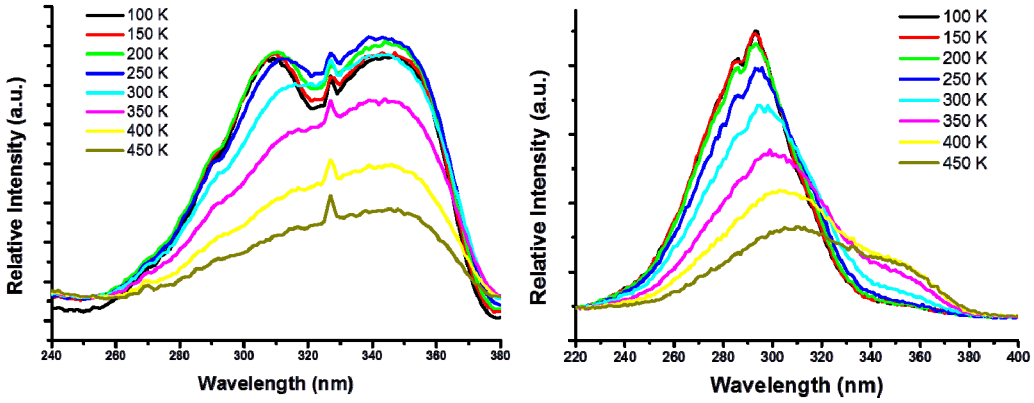

(a) (b)

Fig. S7: Solid-state excitation spectra of **2** monitored by 422 nm (a) and 740 nm (b) under various temperatures. The dependence of excitation spectra on temperature (monitored at 740 nm emission) is similar to the situation of **1** (Fig. S5), except for the shoulders at *ca.* 350 nm, which is probably due to the inter-cluster transition mentioned in the main text (below Fig. 3).

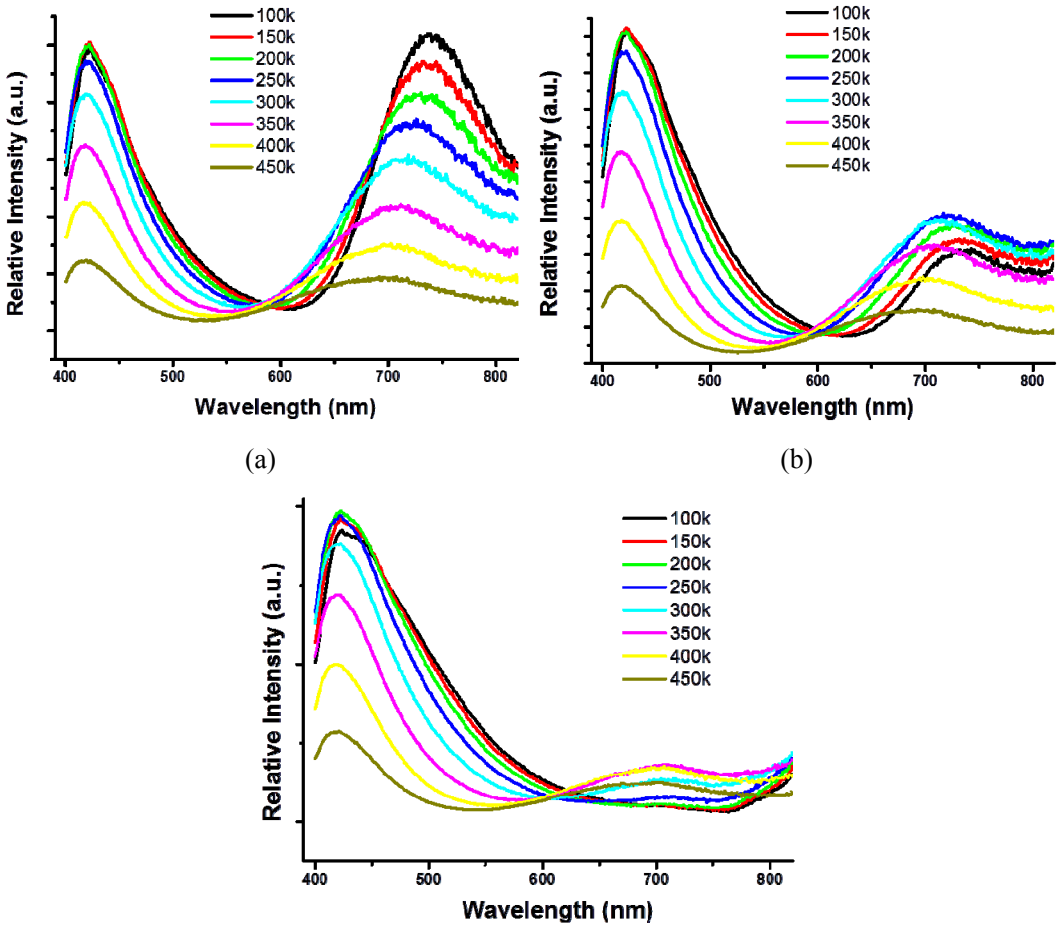

(a) (b)

(c)

Fig. S8: (a) Solid-state emission spectra of **2** upon excited at 290 nm (a), 310 nm (b) and 340 nm (c) upon varying temperature from 100 to 450 K.

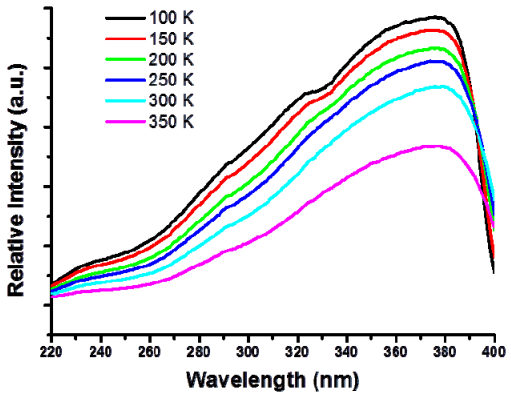

Fig. S9: Solid-state excitation spectra of **3** monitored by 422 nm under various temperatures.

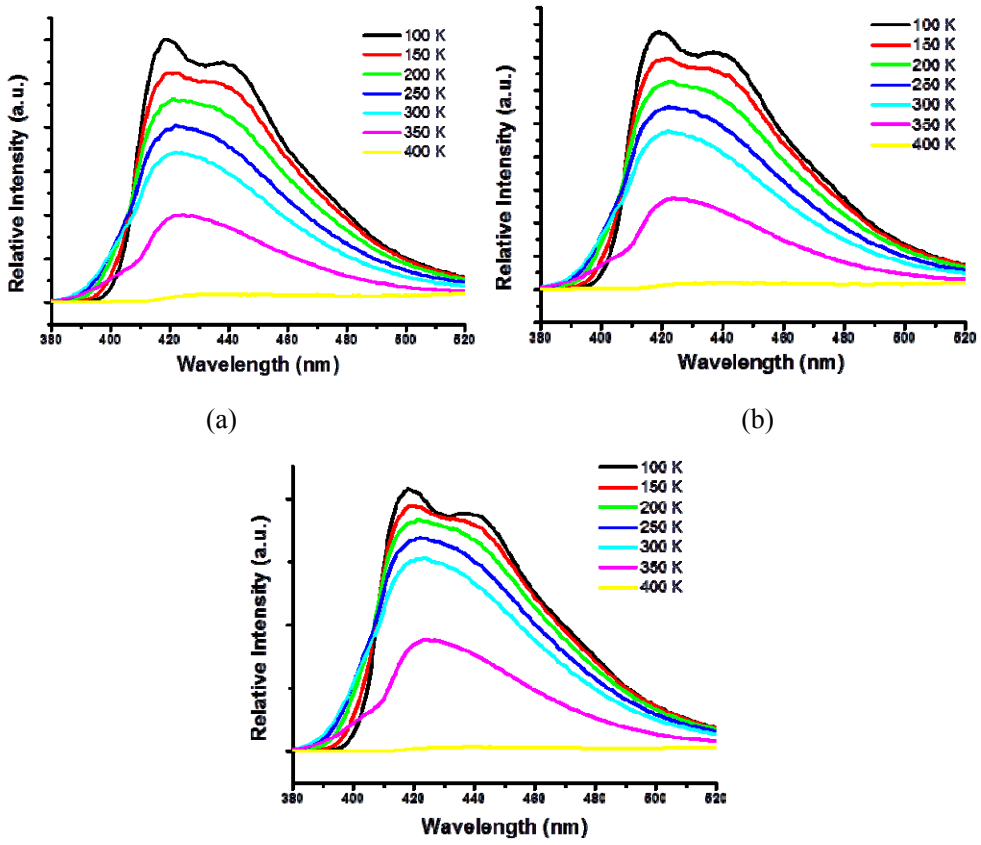

Fig. S10: (a) Solid-state emission spectra of **3** upon excited at 290 nm (a), 310 nm (b) and 340 nm (c) upon varying temperature from 100 to 400 K. Note that at above 350 K the structure of 3 decomposed, and therefore the emission disappeared.

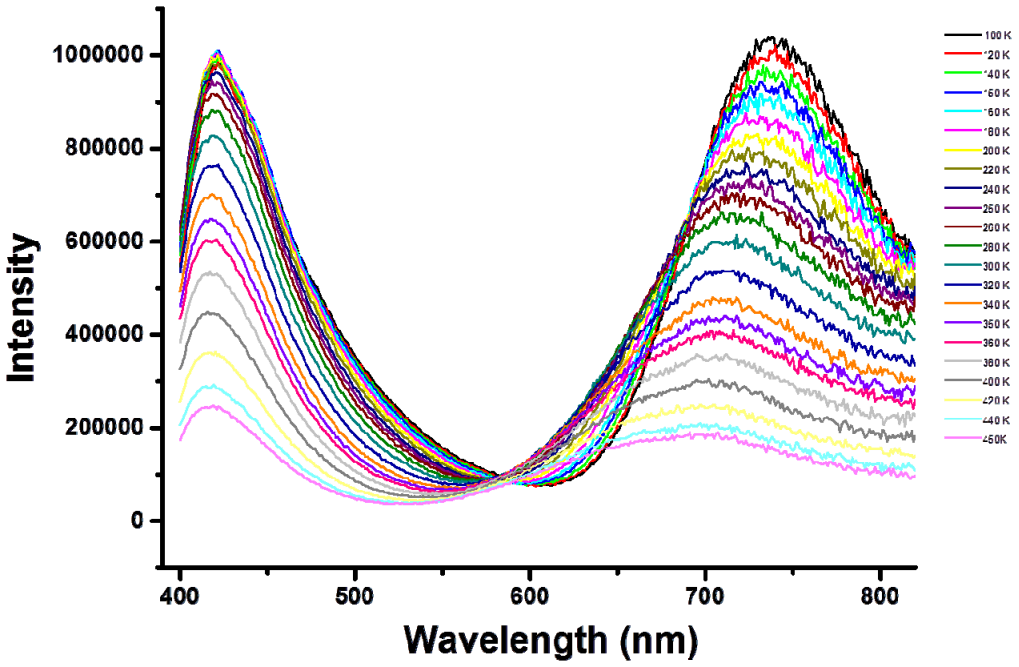
Intensity
1000000
800000
600000
400000
200000
0
400
500
600
700
800
Wavelength (nm)

(a)

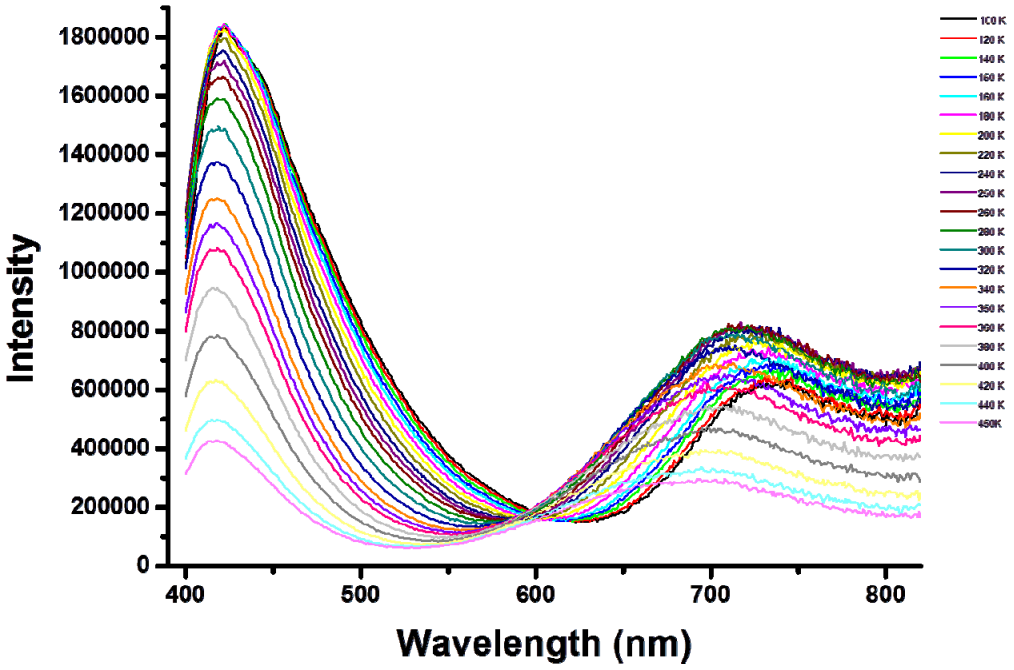
Intensity
1800000
1600000
1400000
1200000
1000000
800000
600000
400000
200000
0
400
500
600
700
800
Wavelength (nm)

(b)

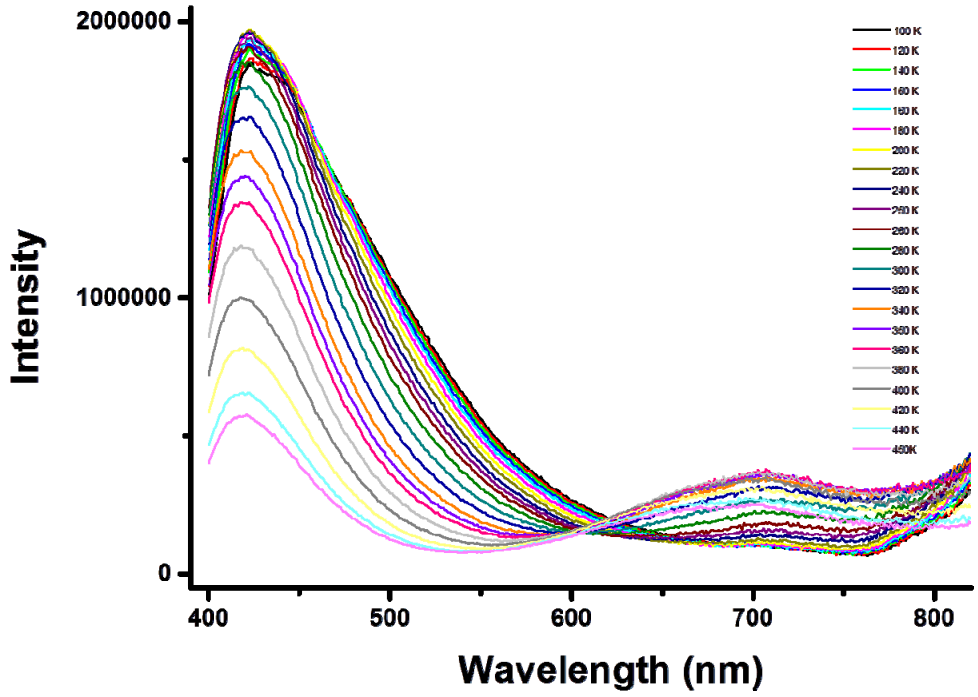

(c)

Fig. S11: (a) Solid-state emission spectra of **2** excited at 290 nm (a), 310 nm (b) and 340 nm (c) recorded at a temperature interval of 20 K from 100 to 450 K.

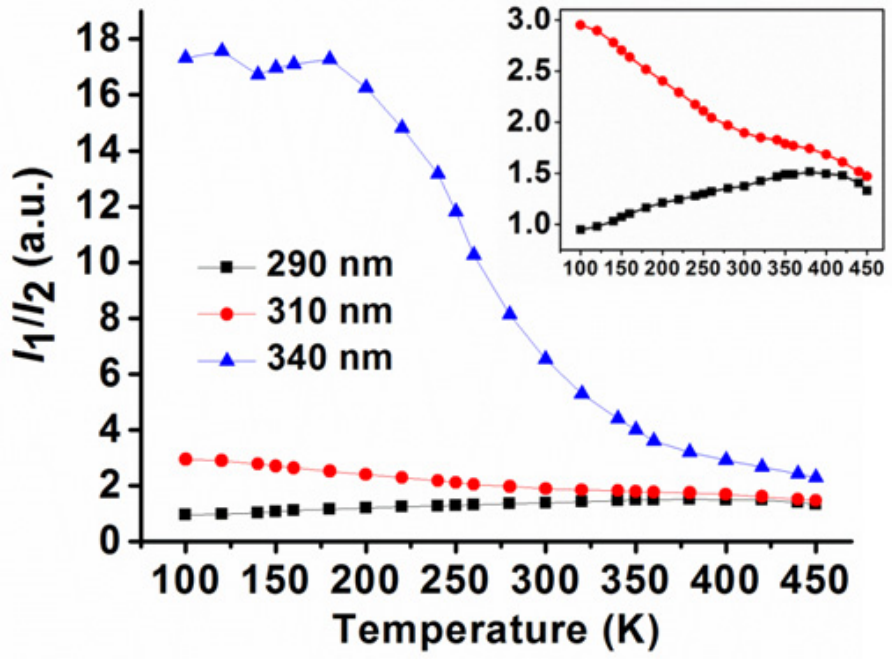

Fig. S12: The relative emission intensity I_1:I_2 of λ^{em}_{max1}:λ^{em}_{max2} excited at three wavelengths with temperature interval of 20 K for **2**. The insert amplifies the data at 290 and 310 nm.

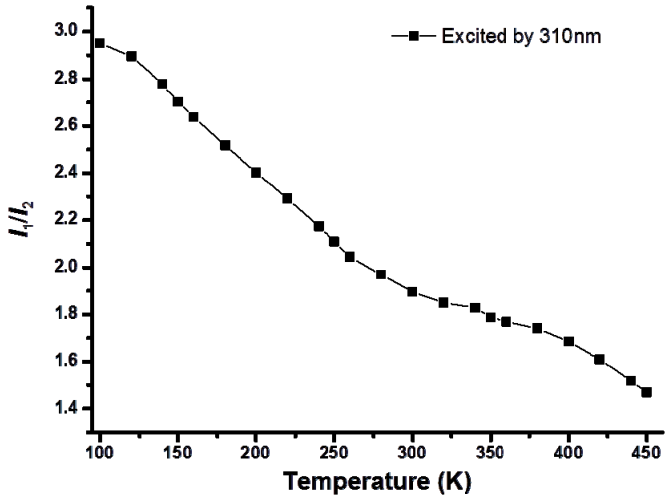

(a)

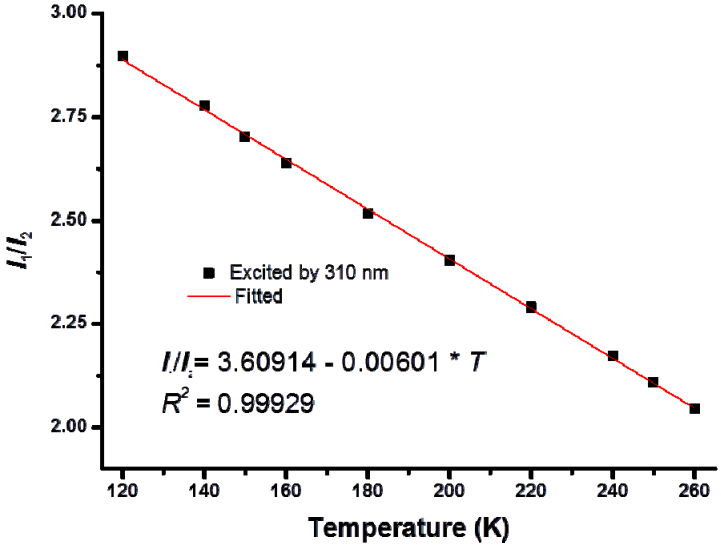

(b)

Fig. S13: The temperature-varied relative emission intensity I_1:I_2 excited at 310 nm for **2** (a) and the linear correlation from 120-260 K (b).

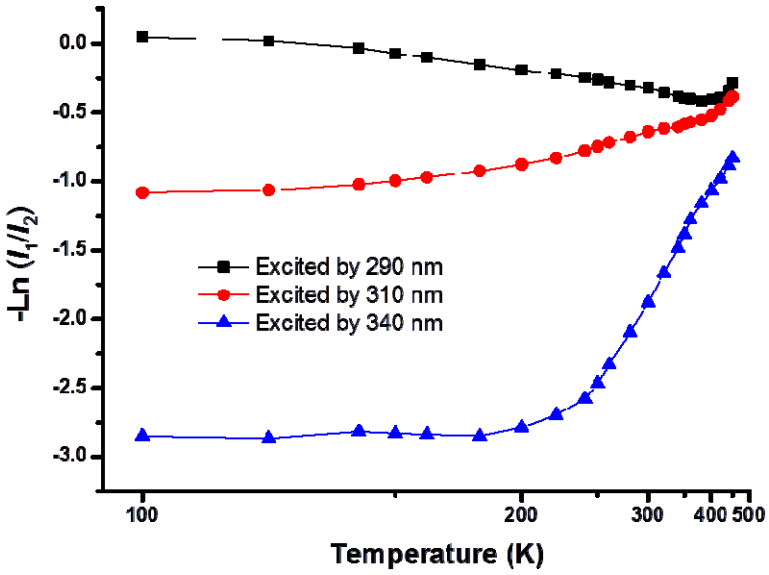

(a)

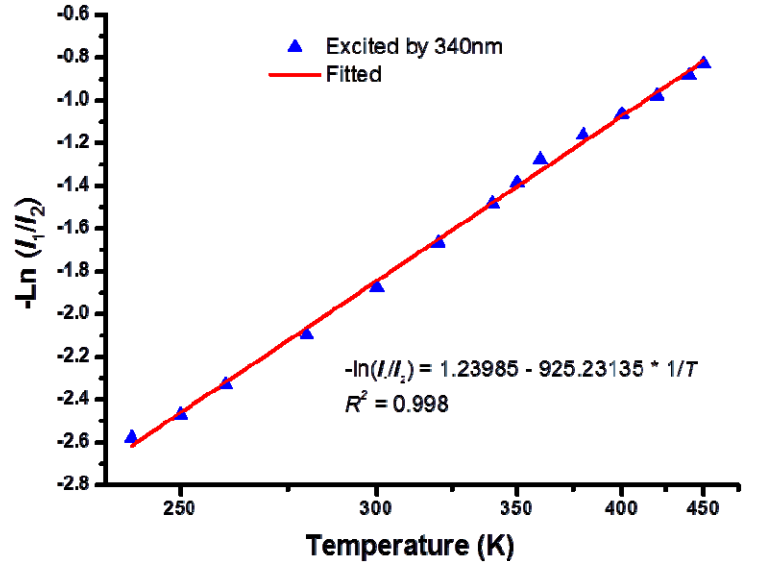

(b)

Fig. S14: The correlation of the relative emission intensity $-\ln(I_1{:}I_2)$ to the temperature (reciprocal coordinate) excited at three wavelengths for **2** (a) and the linear correlation from 240-450 K excited at 340 nm. Note: It can be seen from Fig. S12 that for the 340 nm excitation there is a roughly linear correlation between $I_1{:}I_2$ and temperature in the range of 200-320 K, which exhibits a significantly better sensitivity than those under 290 and 310 nm excitation. However, the linearity is not as good as that shown in Fig. 14b, and therefore we choose to report the $-\ln(I_1{:}I_2) \sim (1/T)$ correlation excited at 340 nm in Fig. 2d in the main text.

Table S3: Lifetimes (τ) of the solid-state samples of 1-3 under varied temperatures and excitation energy.

T (K)	τ/μs **2** (λ^{ex} = 290 nm)	T (K)	τ/μs **1** (λ^{ex} = 290 nm)	T (K)	τ/μs **2** (λ^{ex} = 337 nm)	T (K)	τ/μs **3** (λ^{ex} = 337 nm)
100	13.26949	100	9.58506	100	17.21	100	16.25
125	12.47002	125	9.66927	125	18.54	125	15.99
150	11.47429	150	9.6624	150	16.69	150	15.41
175	11.64065	175	9.13059	175	15.27	175	14.8
200	10.51585	200	9.01998	200	13.08	200	13.32
225	9.4432	225	8.49451	225	11.42	225	12.36
250	8.66224	250	7.94982	250	10.46	250	11.03
275	7.54482	275	7.28027	275	8.96	275	10.17
300	7.568	300	7.12837	300	8.34	300	9.02
325	6.75286	325	6.75154	325	7.12	325	8.13
350	6.5346	350	6.32656	350	6.61	350	7.3
375	5.91465	375	6.01565	375	5.79	375	6.56
400	5.75297	400	5.79024	400	5.54	--	--
425	5.63372	425	5.69315	425	5.17	--	--
450	5.35482	450	5.48756	450	5.1	--	--

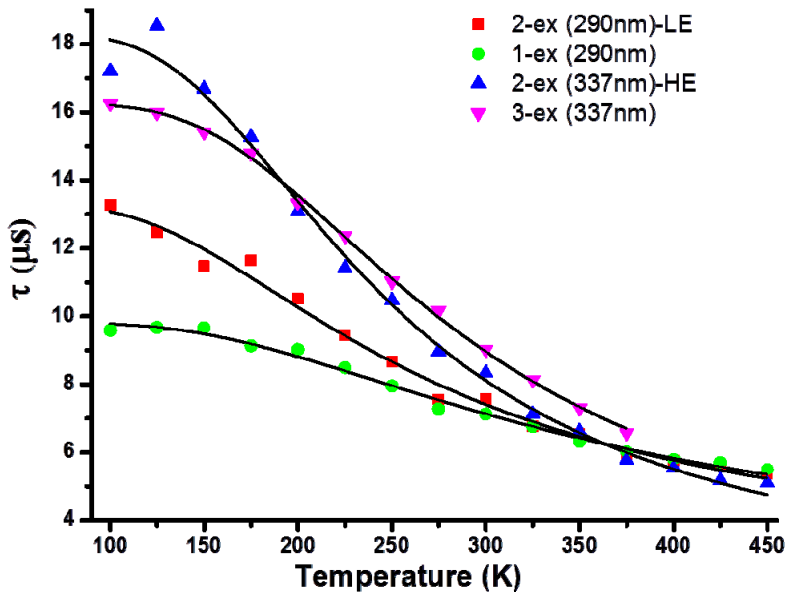

(a)

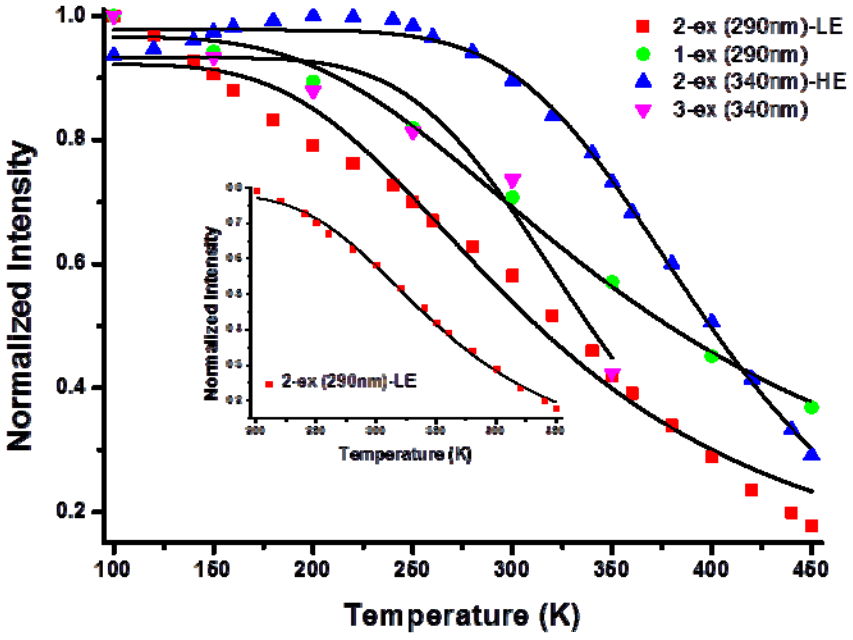

(b)

Fig. S15: (a) The correlation of emission decay lifetimes (a) or emission intensity (b) to temperature (100-450 K) fitted by the Mott-Seitz model. The dots are experimental data, while the black lines are fitted curves. In (b) the inserted picture shows the fitting using the data of **2** from 200-450 K.

Note: The Arrhenius-type equation (Mott-Seitz model) are used to fit the τ-T correlation:[9]

$$\frac{1}{\tau(T)} = \frac{1}{\tau_0} + A \exp\left(-\frac{\Delta E}{k_B T}\right)$$

where τ_0 is the lifetime at T = 0 K, A is the pre-exponential factor, ΔE is the activation energy, and k_B is the Boltzmann constant. The corresponding values of activation energy obtained from the fitting are given below.

ΔE = 512 ± 30 cm^{-1} = 0.0635 ± 0.0037 eV = 6.12 ± 0.36 kJ mol^{-1} (**2**, λ^{ex} = 337 nm)
ΔE = 586 ± 16 cm^{-1} = 0.0726 ± 0.0020 eV = 7.01 ± 0.19 kJ mol^{-1} (**3**, λ^{ex} = 337 nm)
ΔE = 415 ± 29 cm^{-1} = 0.0514 ± 0.0036 eV = 4.96 ± 0.35 kJ mol^{-1} (**2**, λ^{ex} = 290 nm)
ΔE = 500 ± 30 cm^{-1} = 0.0620 ± 0.0037 eV = 5.98 ± 0.36 kJ mol^{-1} (**1**, λ^{ex} = 290 nm)

[9] (a) C. D. S. Brites, P. P. Lima, N. J. O. Silva, A. Millán, V. S. Amaral, F. Palacio, L. D. Carlos, *Adv. Mater.* 2010, **22**, 4499; (b) L. D. Carlos, R. A. S. Ferreira, J. P. Rainho, V. d. Z. Bermudez, *Adv. Funct. Mater.* 2002, **12**, 819.

Computational Section

Density functional theory (DFT) was used in all calculations of complexes **1**, **2** and **3** with the Gaussian 09 A.02 software package.[10] The calculations were carried out using the popular hybrid functional B3LYP with Becke three parameter exchange functional[11] as well as Lee-Yang-Parr correlation functional.[12] The simulated absorption spectra were calculated by time-dependent density functional theory (TD-B3LYP).[13] For comparison, the pure local density functional M06L,[14] which is considered more suitable for systems containing transition metals, was also used for the calculations of **3**. No significant difference was found for the computed orbital composition between B3LYP and M06L. Therefore the results using M06L are not reported here.

The models for calculations were taken from the X-ray single-crystal diffraction data of **1**, **2** and **3**, respectively. In all calculations, the combined basis set SDD+6-311g** was used, specifically, with the Stuttgart-Dresden triple-ζ quality basis set (SDD) with a quasi-relativistic effective core potential (ECP)[15] for Cu and I, and the Pople's polarized triple-ζ split valence basis set (6-311g**)[16,17] for C, N and H. The molecular orbital compositions were analyzed mainly by the Hirshfeld method,[18,19] as well as the NAO method.[20] The composition data from both methods were obtained using the software MultiWFN 2.6.1.[21] The authors wish to thank Tian Lu at the University of Science and Technology Beijing for the discussion on Hirshfeld analysis and the usage of MultiWFN,[19,21] which is available at http://multiwfn.codeplex.com/.

[10] M. J. Frisch, G. W. Trucks, H. B. Schlegel, G. E. Scuseria, M. A. Robb, J. R. Cheeseman, G. Scalmani, V. Barone, B. Mennucci, G. A. Petersson, H. Nakatsuji, M. Caricato, X. Li, H. P. Hratchian, A. F. Izmaylov, J. Bloino, G. Zheng, J. L. Sonnenberg, M. Hada, M. Ehara, K. Toyota, R. Fukuda, J. Hasegawa, M. Ishida, T. Nakajima, Y. Honda, O. Kitao, H. Nakai, T. Vreven, J. A. Montgomery, Jr., J. E. Peralta, F. Ogliaro, M. Bearpark, J. J. Heyd, E. Brothers, K. N. Kudin, V. N. Staroverov, R. Kobayashi, J. Normand, K. Raghavachari, A. Rendell, J. C. Burant, S. S. Iyengar, J. Tomasi, M. Cossi, N. Rega, J. M. Millam, M. Klene, J. E. Knox, J. B. Cross, V. Bakken, C. Adamo, J. Jaramillo, R. Gomperts, R. E. Stratmann, O. Yazyev, A. J. Austin, R. Cammi, C. Pomelli, J. Ochterski, R. L. Martin, K. Morokuma, V. G. Zakrzewski, G. A. Voth, P. Salvador, J. J. Dannenberg, S. A. D. Dapprich, O. Daniels, J. B. Farkas, J. V. Foresman, O. J. Cioslowski, D. J. Fox, GAUSSIAN 09 (Revision A.2), Gaussian, Inc., Wallingford, CT, 2009. Frisch, M. J. et al, GAUSSIAN 09 (Revision A.02), Gaussian, Inc., Wallingford, CT, 2009.

[11] A. D. Becke, *J. Chem. Phys.* 1993, **98**, 5648.

[12] C. Lee, W. R. Yang, G. Parr, *Phys. Rev.* 1988, **B37**, 785.

[13] K. Burke, E. K. U. Gross, A guided tour of time-dependent density functional theory. In Density Functionals: Theory and Applications, Lecture Notes in Physics; Joubert, D., Ed.; Springer: New York, 1998; Vol. 500.

[14] Y. Zhao, D. G. Truhlar, *Acc. Chem. Res.* 2008, 41, 157.

[15] W. Kuechle, M. Dolg, H. Stoll, H. Preuss, *J. Chem. Phys.* 1994, **100**, 7535.

[16] R. Krishnan, J. S. Binkley, R. Seeger, J. A. Pople, *J. Chem. Phys.* 1980, **72**, 650.

[17] A. D. McLean, G. S. Chandler, *J. Chem. Phys*. 1980, **72**, 5639.

[18] F. L. Hirshfeld, *Theor. Chim. Acta (Berl.)* 1977, **44**, 129.

[19] T. Lu, F. W. Chen, *Acta Chim. Sin.* 2011, **69**, 2393.

[20] (a) A. E. Reed, F. Weinhold, *J. Chem. Phys.* 1983, **78**, 4066. (b) A. E. Reed, R. B. Weinstock, F. Weinhold, *J. Chem. Phys.* 1985, **83**, 735.

[21] (a) T. Lu, F. W. Chen, *J. Comp. Chem.* 2012, **33**, 580. (b) T. Lu, Multiwfn, Revison 2.6.1; University of Science and Technology Beijing: Beijing, China, 2013.

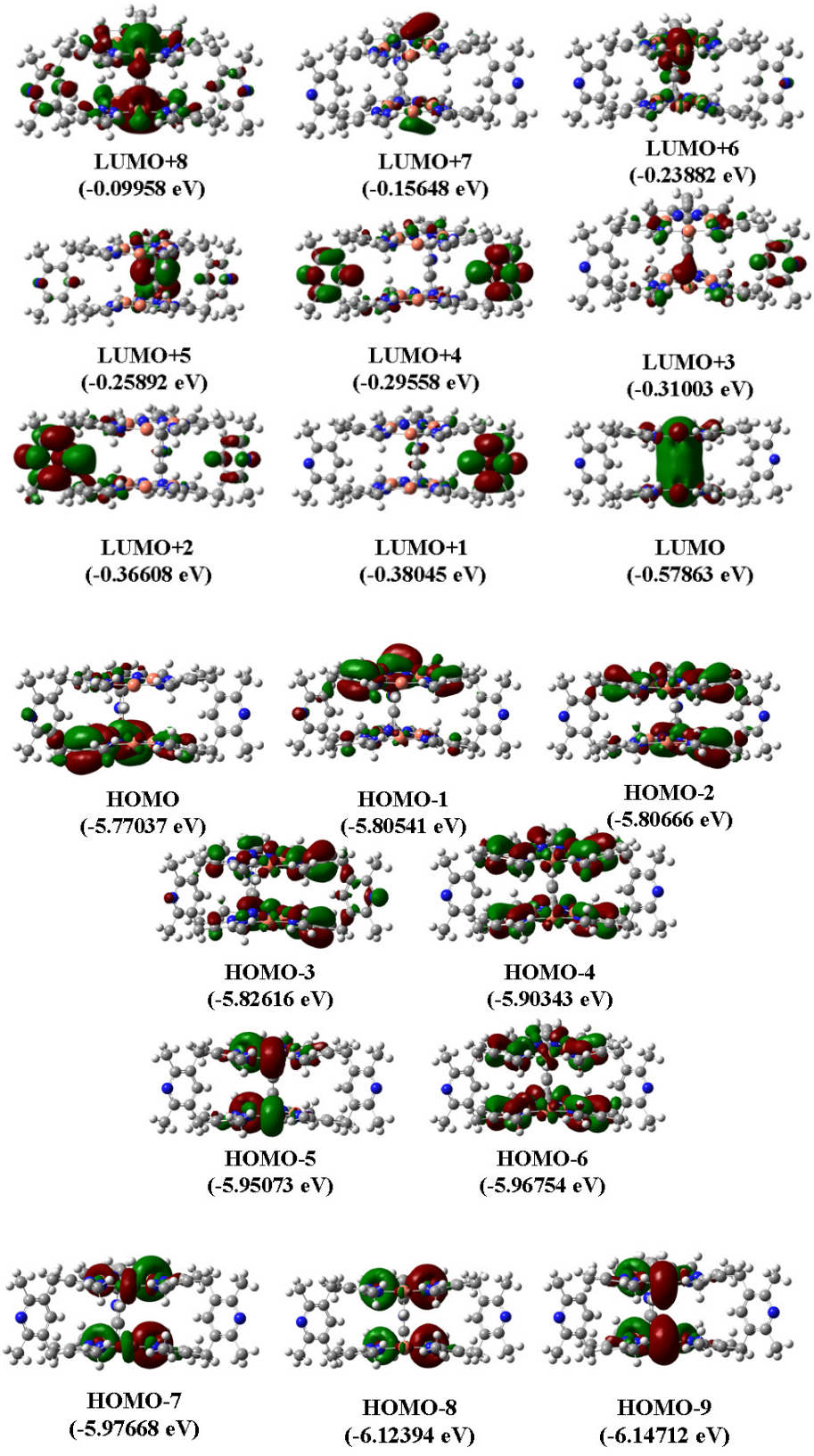
LUMO+8
(-0.09958 eV)
LUMO+7
(-0.15648 eV)
LUMO+6
(-0.23882 eV)
LUMO+5
(-0.25892 eV)
LUMO+4
(-0.29558 eV)
LUMO+3
(-0.31003 eV)
LUMO+2
(-0.36608 eV)
LUMO+1
(-0.38045 eV)
LUMO
(-0.57863 eV)
HOMO
(-5.77037 eV)
HOMO-1
(-5.80541 eV)
HOMO-2
(-5.80666 eV)
HOMO-3
(-5.82616 eV)
HOMO-4
(-5.90343 eV)
HOMO-5
(-5.95073 eV)
HOMO-6
(-5.96754 eV)
HOMO-7
(-5.97668 eV)
HOMO-8
(-6.12394 eV)
HOMO-9
(-6.14712 eV)

(a)

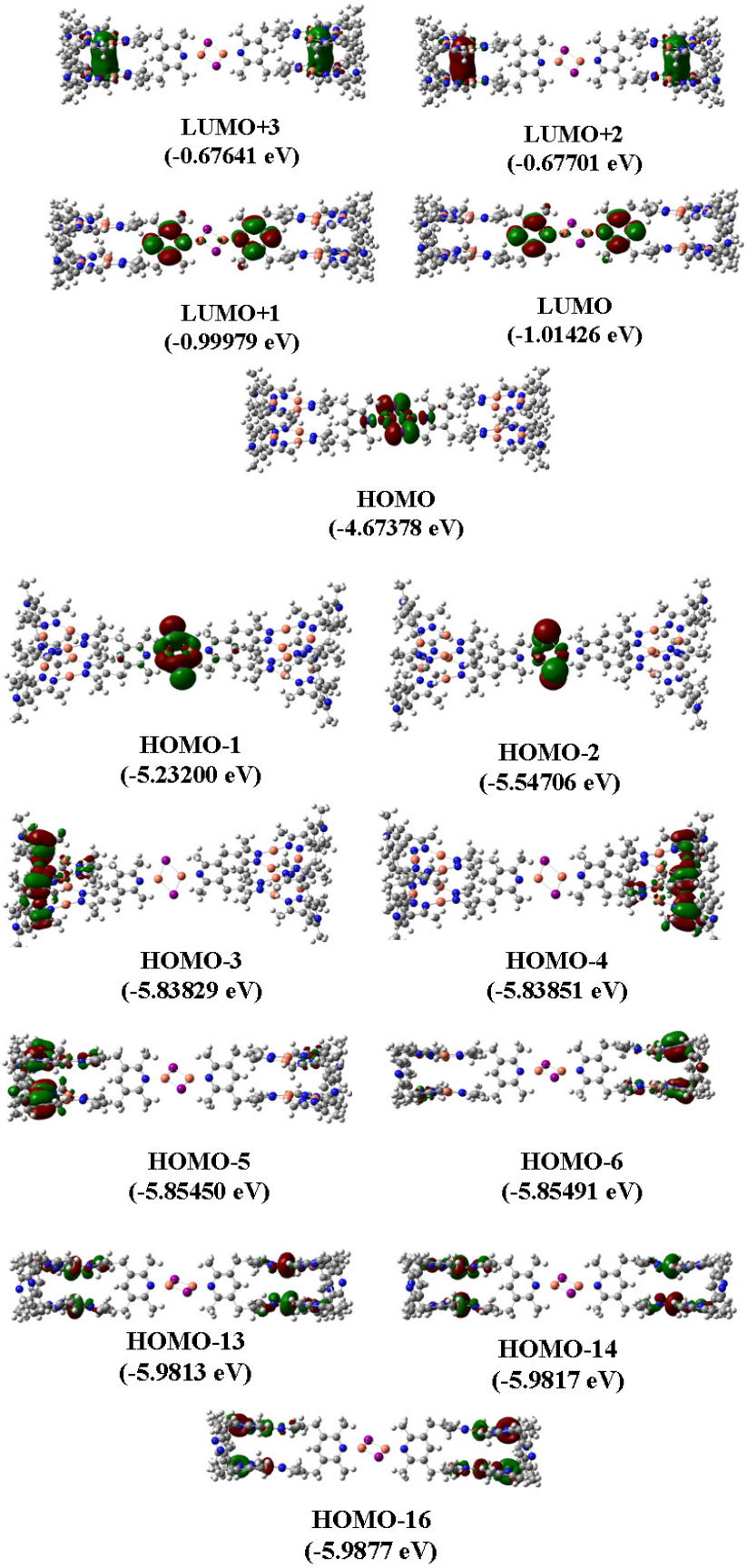
LUMO+3
(-0.67641 eV)
LUMO+2
(-0.67701 eV)
LUMO+1
(-0.99979 eV)
LUMO
(-1.01426 eV)
HOMO
(-4.67378 eV)
HOMO-1
(-5.23200 eV)
HOMO-2
(-5.54706 eV)
HOMO-3
(-5.83829 eV)
HOMO-4
(-5.83851 eV)
HOMO-5
(-5.85450 eV)
HOMO-6
(-5.85491 eV)
HOMO-13
(-5.9813 eV)
HOMO-14
(-5.9817 eV)
HOMO-16
(-5.9877 eV)

(b)

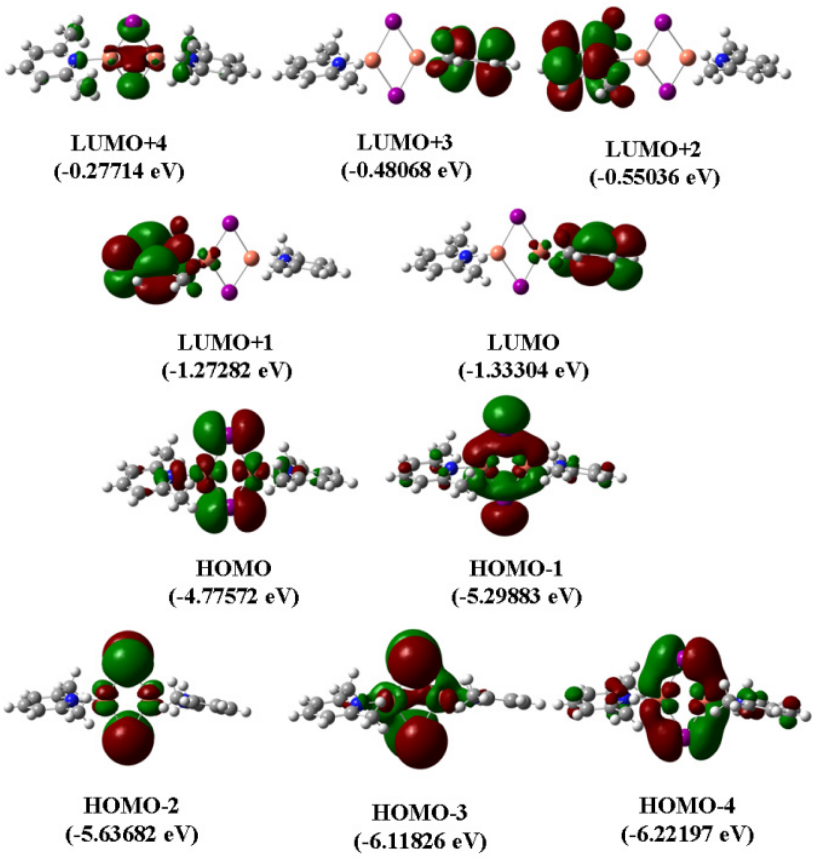

(c)

Fig. S16: Selected frontier molecular orbital contours and energy levels for **1** (a)**, 2** (b) and **3** (c) at the B3LYP/(SDD+6-311g**) level (isovalue = 0.02). Further quantitative descriptions of MOs are given below.

After careful examination of the orbital contours (Fig. S16), the characteristic frontier molecular orbitals of **1** and **3** are found to exhibit the following one-to-one correspondence with those of **2**:

1		**2**		**3**
LUMO	←	LUMO+3		
		LUMO+2		
		LUMO+1	→	LUMO+1
		LUMO	→	LUMO
		HOMO	→	HOMO
		HOMO-1	→	HOMO-1
		HOMO-2	→	HOMO-2
HOMO	←	HOMO-3		
		HOMO-4		
HOMO-1	←	HOMO-5		
		HOMO-6		

Note the HOMO-5/-6, HOMO-3/-4 and LUMO+2/+3 orbitals are degenerate because there are two equivalent $Cu_6\mathbf{L}_3$ cages in **2**. Table S4 and S5 compare quantitatively the Hirshfeld/NAO orbital compositions of these counterparts of frontier molecular orbitals.

Table S4: Comparison of Hirshfeld (and NAO) percentage (B3LYP/(SDD+6-311g**) level) of orbital compositions of the counterparts of frontier molecular orbitals in **2** and **3**. Cu for **2** refers to the two copper atoms coordinated to iodine atoms. py for **2** refers to the 2,6-dimethyl-pyridyl groups in the ligands connected to the Cu_2I_2 cluster and for **3** refers to the whole ligands.

	%	HOMO-2	HOMO-1	HOMO	LUMO	LUMO+1
2	Cu	36.11 (31.12)	51.70 (46.76)	54.95 (50.37)	3.35 (3.17)	2.65 (1.86)
	I	62.70 (68.76)	41.89 (49.03)	36.15 (39.50)	1.56 (1.08)	0.85 (0.48)
	py	1.18 (0.11)	6.22 (4.13)	8.44 (9.73)	87.64 (92.40)	88.93 (94.24)
	Others	0.01 (0.01)	0.19 (0.08)	0.46 (0.40)	7.45 (3.35)	7.57 (3.41)
3	Cu	35.84 (30.83)	50.76 (45.53)	55.29 (50.45)	3.38 (2.61)	3.43 (2.61)
	I	63.06 (69.01)	42.65 (50.03)	36.14 (39.56)	1.47 (1.03)	1.51 (1.10)
	py	1.10 (0.16)	6.58 (4.44)	8.57 (9.98)	95.15 (96.36)	95.06 (96.29)
		HOMO-2	HOMO-1	HOMO	LUMO	LUMO+1

Note: The percentage values given in the parentheses are from NAO analysis for comparison. In higher-energy absorption transitions the high-lying unoccupied orbitals may be involved, but the Rydberg composition of high-lying unoccupied orbitals could be so high that the NAO method is no longer reliable. Therefore the Hirshfeld method is used in the analysis of the UV-vis spectra.

Table S5: Comparison of Hirshfeld (and NAO) percentage (B3LYP/(SDD+6-311g**) level) of orbital compositions of the counterparts of frontier molecular orbitals in **2** and **1**. Cu for **2** refers to the copper atoms coordinated to the pyrazolyl groups. L = ligand.

	%	HOMO-6	HOMO-5	HOMO-4	HOMO-3	LUMO+2	LUMO+3
2	Cu	25.69 (24.01)	25.68 (24.00)	24.59 (23.12)	24.60 (23.12)	61.41 (85.15)	61.24 (85.56)
	L	74.28 (75.95)	74.25 (75.93)	75.40 (76.87)	75.39 (76.87)	38.29 (14.33)	38.19 (14.39)
	Cu_2I_2	0.04 (0.04)	0.07 (0.07)	0.01 (0.01)	0.01 (0.01)	0.29 (0.52)	0.57 (0.05)
1	Cu	25.54 (23.90)		25.10 (23.48)		61.16 (86.40)	
	L	74.46 (76.10)		74.90 (76.52)		38.84 (13.60)	
		HOMO-1		HOMO		LUMO	

The results in Table S4 and S5 offer a quantitative description of the molecular orbitals. For example, LUMO and LUMO+1 of **2** are dominantly (over 85 %) based on the π* orbitals of the pyridine ligand, which correspond to the LUMO and LUMO+1 of **3** (with an almost exclusive contribution of 95%). The degenerate LUMO+2 and LUMO+3 of **2** are mainly (over 60 %) based on the delocalized density of Cu within the cage, similar to the situation of LUMO of **1** (with a contribution of 61.16 % from Cu). The percentage compositions of the counterparts of corresponding frontier molecular orbitals are very close, indicating the characteristic molecular orbitals of **1** and **3** are well preserved in those of **2**. The Hirshfeld percentages are then used in the absorption transition analysis of **1**-**3** calculated from TD-DFT method, shown in Table S6, S7 and S8, respectively. In the calculations of absorption transitions, the spin-allowed transitions (first 20 for **1**, first 40 for **2**, first 50 for **3**) have been computed. The major excitation transitions (largest oscillator strengths and largest percentages) are reported in Fig. 3 in the main text.

Table S6: The first 20 lowest energy transitions and their oscillator strength (*f*) for complex **1** at the (TD-)B3LYP/(SDD+6-311g**) level. The major excitation transitions are marked in red.

No.	λ(nm)	eV	oscillator strength (*f*)	Assignment (H = HOMO, L = LUMO)
1	283.2	4.38	0	H→L (74%), H→L+6 (6%), H→L+8 (6%)
2	281.7	4.4	0.0008	H-1→L (52%), H-2→L (19%), H-1→L+6 (6%)
3	281	4.41	0.0001	H-2→L (40%), H-1→L (18%), H-3→L (14%)
4	279.5	4.44	0.0006	H-3→L (55%), H-2→L (15%), H-2→L+8 (5%)
5	276.3	4.49	0.0003	H-4→L (68%), H-4→L+6 (7%)
6	273.4	4.54	0.0005	H-6→L (52%), H-5→L (15%), H-4→L+8 (7%), H-6→L+6 (5%)
7	271.4	4.57	0.0007	H-5→L (65%), H-6→L (16%)
8	269.8	4.6	0.0004	H-7→L (82%)
9	263.4	4.71	0.0197	H-8→L (33%), H-9→L (24%), H-5→L+8 (6%)
10	262.9	4.72	0.0191	H-8→L (33%), H-9→L (29%), H-7→L+8 (6%)
11	259.9	4.77	0.0155	H→L+2 (22%), H-1→L+2 (10%), H-3→L+2 (10%), H-9→L (8%)
12	258.5	4.8	0.0157	H-3→L+1 (40%), H-3→L+4 (8%)
13	256.8	4.83	0.0015	H-2→L+1 (14%), H-2→L+2 (11%), H→L+4 (9%), H→L+3 (7%), H-2→L+3 (6%), H-1→L+4 (6%)
14	256.6	4.83	0.0011	H-2→L+1 (20%), H→L+6 (6%), H-2→L+6 (5%), H-2→L+3 (5%)
15	256	4.84	0.0008	H→L+4 (13%), H→L+6 (9%), H→L+2 (8%), H-2→L+1 (7%), H→L+1 (6%),H→L (5%)
16	255.2	4.86	0.0001	H-1→L+6 (14%), H-1→L+4 (12%), H-1→L (11%), H-1→L+3 (9%), H-1→L+7 (6%), H→L+7 (6%)
17	254.8	4.87	0.0065	H-3→L+6 (11%), H-2→L+7 (7%), H-3→L+3 (7%), H-3→L (7%), H-1→L+1 (7%), H-3→L+4 (7%), H-3→L+1 (7%)
18	254.7	4.87	0.0159	H-1→L+5 (16%), H-3→L+5 (8%), H→L+5 (8%)
19	253.2	4.9	0.0017	H→L+3 (10%), H-3→L+6 (7%), H-2→L+4 (6%)
20	253	4.9	0.0016	H→L+2 (19%), H-2→L+4 (15%), H-1→L+2 (9%), H-2→L+3 (8%)

Table S7: The first 40 lowest energy transitions and their oscillator strength (*f*) for complex **2** at the (TD-)B3LYP/(SDD+6-311g**) level. The major excitation transitions are marked in red.

No.	λ(nm)	eV	oscillator strength(*f*)	Assignment (H = HOMO, L = LUMO)
1	421.9	2.94	0	H→L (98%)
2	416.7	2.98	0.0032	H→L+1 (98%)
3	342.7	3.62	0.1439	H-1→L+1 (+78%), H→L+4(6%)
4	340	3.65	0	H-1→L (98%)
5	336.6	3.68	0.1657	H→L+3 (27%), H→L+4 (20%), H-1→L+1(19%), H→L+8 (15%), H→L+20 (9%)
6	335.4	3.7	0	H→L+7 (53%), H→L+9 (40%)
7	335.1	3.7	0.003	H→L+6 (54%), H→L+10 (30%), H→L+8 (8%)
8	330.6	3.75	0	H→L+2 (96%)
9	327.6	3.78	0.036	H→L+3 (70%), H→L+8 (9%), H→L+4 (9%), H→L+20 (5%)
10	318.4	3.89	0.0021	H-2→L (97%)
11	316.8	3.91	0	H-2→L+1 (97%)
12	308.6	4.02	0	H→L+5 (41%), H→L+11 (26%), H→L+9 (11%), H→L+7 (7%), H→L+13 (7%)
13	304.7	4.07	0.0006	H→L+10 (61%), H→L+6 (16%), H→L+4 (12%), H→L+8 (9%)
14	304.4	4.07	0	H→L+9 (40%), H→L+7 (27%), H→L+11 (26%), H→L+13 (5%)
15	301.1	4.12	0.0021	H→L+4 (49%), H→L+6 (16%), H→L+20 (12%), H→L+10 (7%), H→L+8 (5%)
16	299.6	4.14	0	H→L+5 (56%), H→L+11 (23%), H→L+7 (9%), H→L+9 (5%), H→L+13 (5%)
17	297.8	4.16	0.0007	H→L+8 (48%), H→L+20 (23%), H→L+6 (11%), H→L+24 (6%)
18	296.4	4.18	0	H→L+13 (56%), H→L+15 (21%), H→L+19 (8%), H→L+11 (8%)
19	296.4	4.18	0.0002	H→L+12 (63%), H→L+14 (22%), H→L+18 (8%)
20	294.6	4.21	0	H→L+15 (66%), H→L+13 (18%), H→L+11 (12%)
21	294.6	4.21	0.0006	H→L+14 (68%), H→L+12 (28%)
22	291.4	4.25	0	H→L+17 (85%), H→L+22 (6%)
23	291.1	4.26	0.0001	H→L+16 (85%)
24	290.6	4.27	0.0282	H-1→L+3 (51%), H-1→L+8 (16%), H-1→L+4 (16%), H-1→L+20 (6%)
25	289.9	4.28	0	H-1→L+7 (48%), H-1→L+9 (37%)
26	289.6	4.28	0.005	H-1→L+6 (49%), H-1→L+10 (27%), H-1→L+4 (6%)
27	288.8	4.29	0	H→L+19 (81%), H→L+15 (6%)
28	288.7	4.3	0.0003	H→L+18 (83%), H→L+14 (6%)
29	287.7	4.31	0	H-1→L+2 (93%)
30	286.8	4.32	0	H-19→L (56%), H-26→L+1 (13%), H-8→L (7%), H-7→L+1 (6%)

31	286.6	4.33	0.0507	H-19→L+1 (46%), H-26→L (17%), H-7→L (8%), H-8→L+1 (8%)
32	285.6	4.34	0	H→L+21 (92%)
33	285.1	4.35	0.0079	H-9→L (20%), H-7→L (15%), H-8→L+1 (15%), H-10→L+1 (13%), H-25→L+1 (7%)
34	285	4.35	0	H-9→L+1 (19%), H-8→L (17%), H-7→L+1 (15%), H-10→L (15%), H-25→L (7%)
35	284.6	4.36	0.0016	H→L+24 (62%), H→L+20 (24%), H→L+23 (10%)
36	284.6	4.36	0.0016	H-3→L+2 (30%), H-3→L+3(27%), H-4→L+3(12%), H-4→L+2 (7%)
37	284.6	4.36	0.0001	H-4→L+2 (33%), H-4→L+3 (25%), H-3→L+3 (12%), H-3→L+2 (7%)
38	284.1	4.36	0.0297	H-1→L+3 (32%), H-1→L+4 (16%), H-1→L+8 (12%), H-1→L+20(6%)
39	283.9	4.37	0	H→L+25 (46%), H→L+22 (26%), H→L+30 (7%)
40	283.5	4.37	0.0003	H→L+26 (49%), H→L+23 (16%)

Table S8: The first 50 lowest energy transitions and their oscillator strength (*f*) for complex **3** at the (TD-)B3LYP/(SDD+6-311g**) level. The major excitation transitions are marked in red.

No.	λ(nm)	eV	oscillator strength (f)	Assignment (H = HOMO, L = LUMO)
1	456.9	2.71	0.0013	H→L (92%), H→L+1 (6%)
2	447.2	2.77	0.0025	H→L+1 (92%), H→L (6%)
3	364.6	3.4	0.1118	H-1→L (91%), H-1→L+1 (7%)
4	356.3	3.48	0.034	H-1→L+1 (91%), H-1→L (8%)
5	347.9	3.56	0	H→L+2 (99%)
6	341.1	3.63	0.0001	H→L+3 (99%)
7	339.5	3.65	0.0012	H-2→L (97%)
8	334.2	3.71	0.0014	H-2→L+1 (97%)
9	326.5	3.8	0.0534	H→L+4 (91%), H→L+6 (6%)
10	304.4	4.07	0.0037	H-3→L (74%), H-7→L (13%), H-5→L (7%)
11	300.7	4.12	0.0007	H-1→L+2 (97%)
12	300.3	4.13	0.0011	H-3→L+1 (73%), H-7→L+1 (12%), H-5→L+1 (8%)
13	296.1	4.19	0.0001	H-5→L (47%), H-6→L (34%), H-8→L (6%), H-7→L (6%)
14	295.9	4.19	0.0006	H-1→L+3 (95%)
15	293.4	4.23	0.0004	H→L+5 (95%)
16	292.7	4.24	0.0004	H-5→L+1 (53%), H-6→L+1 (24%), H-7→L+1 (12%), H-8→L+1 (6%)
17	288	4.31	0.0798	H-4→L (84%), H-3→L (6%)
18	284.2	4.36	0.0503	H-4→L+1(85%),H-3→L+1(5%)
19	282.6	4.39	0.0802	H-1→L+4 (95%)
20	280.9	4.41	0.0026	H-7→L (38%), H-6→L (19%), H-5→L (16%), H-3→L (12%), H-8→L (7%)
21	277.3	4.47	0.0043	H-7→L+1 (49%), H-5→L+1 (14%), H-3→L+1 (12%),

				H-6→L+1 (8%), H-8→L+1 (7%), H-4→L+1 (5%)
22	275.8	4.5	0.0044	H-2→L+2 (96%)
23	273.7	4.53	0.0017	H-7→L (34%), H-6→L (32%), H-8→L (22%)
24	271.8	4.56	0.0018	H-2→L+3 (98%)
25	270.5	4.58	0	H-6→L+1 (46%), H-8→L+1 (27%), H-7→L+1 (18%)
26	268.4	4.62	0	H-9→L (77%), H→L+7 (6%)
27	267.2	4.64	0	H-0→L+7 (68%), H→L+6 (12%), H-9→L (11%)
28	266	4.66	0.0011	H-2→L+4 (89%), H-2→L+6 (5%)
29	265.3	4.67	0.0003	H-9→L+1 (81%)
30	264.5	4.69	0.0003	H-8→L (62%), H-5→L (22%), H-6→L (10%)
31	264	4.7	0.0088	H→L+6 (69%), H→L+7 (16%), H→L+4(5%)
32	261.5	4.74	0.0001	H-8→L+1 (58%), H-5→L+1 (22%), H-6→L+1 (17%)
33	261.1	4.75	0	H-1→L+5 (99%)
34	251.2	4.94	0	H-3→L+2 (87%), H-7→L+2 (6%)
35	249.1	4.98	0.0009	H-10→L (92%)
36	248	5	0.0002	H-3→L+3 (85%), H-7→L+3 (7%)
37	246.9	5.02	0.0006	H-4→L+2 (85%)
38	246.2	5.04	0.001	H-10→L+1 (88%)
39	245.3	5.05	0.0009	H→L+8 (90%)
40	244.1	5.08	0	H-5→L+2 (57%), H-6→L+2 (27%), H-7→L+2 (9%)
41	243.7	5.09	0.0009	H-4→L+3 (82%), H-14→L (7%)
42	243.4	5.09	0	H-2→L+5 (99%)
43	240.6	5.15	0.0223	H-3→L+4 (54%), H-5→L+3 (21%), H-6→L+3 (15%)
44	240.6	5.15	0.014	H-3→L+4 (35%), H-5→L+3 (32%), H-6→L+3 (22%)
45	238.6	5.2	0.0042	H-1→L+7 (83%), H-1→L+6 (7%)
46	238.2	5.21	0.0063	H→L+9 (75%), H-4→L+4 (7%)
47	237.2	5.23	0.0004	H-4→L+4 (74%), H-4→L+6 (7%), H→L+9 (6%), H→L+8 (5%)
48	235.1	5.27	0.0003	H-7→L+2 (60%), H-5→L+2 (16%), H-6→L+2 (9%), H-3→L+2 (7%)
49	233.6	5.31	0.0794	H-1→L+6 (76%), H-2→L+7 (9%), H-1→L+7 (7%)
50	232.7	5.33	0.0014	H-11→L (52%), H-12→L (31%)

The corresponding major excitation transitions in the simulated transitions of **1**-**3** (experimentally **1** at 290 nm, **3** at 310 and 340 nm; **2** is the combination of both) are marked in red in Table S6-S8. The calculated spin-allowed absorption transitions are in good agreement with the experimental UV-vis absorption spectra (Fig. S4 and S17), except for the blue shifts of the simulated peaks compared with those of experimental absorption spectra. This is reasonable because of the overestimate of excitation energies at the TD-B3LYP level and the crystalline cooperative effects. The experimental absorption spectral features of **1**-**3**, such as the spectral shoulders of **1** and **2**, and the broad band absorption of **3**, are observed in the simulated spectra. We note that the first 40 spin-allowed transitions of **2** still cannot cover the whole experimental UV-vis absorption spectra, and also the orbital contours and orbital compositions of low-lying HOMO-13 to HOMO-16 of **2** are very similar to those of HOMO-7 to HOMO-9 of **1**. These low-lying HOMOs are involved in the strongest excitation transitions of **1**, as shown in Table S6.

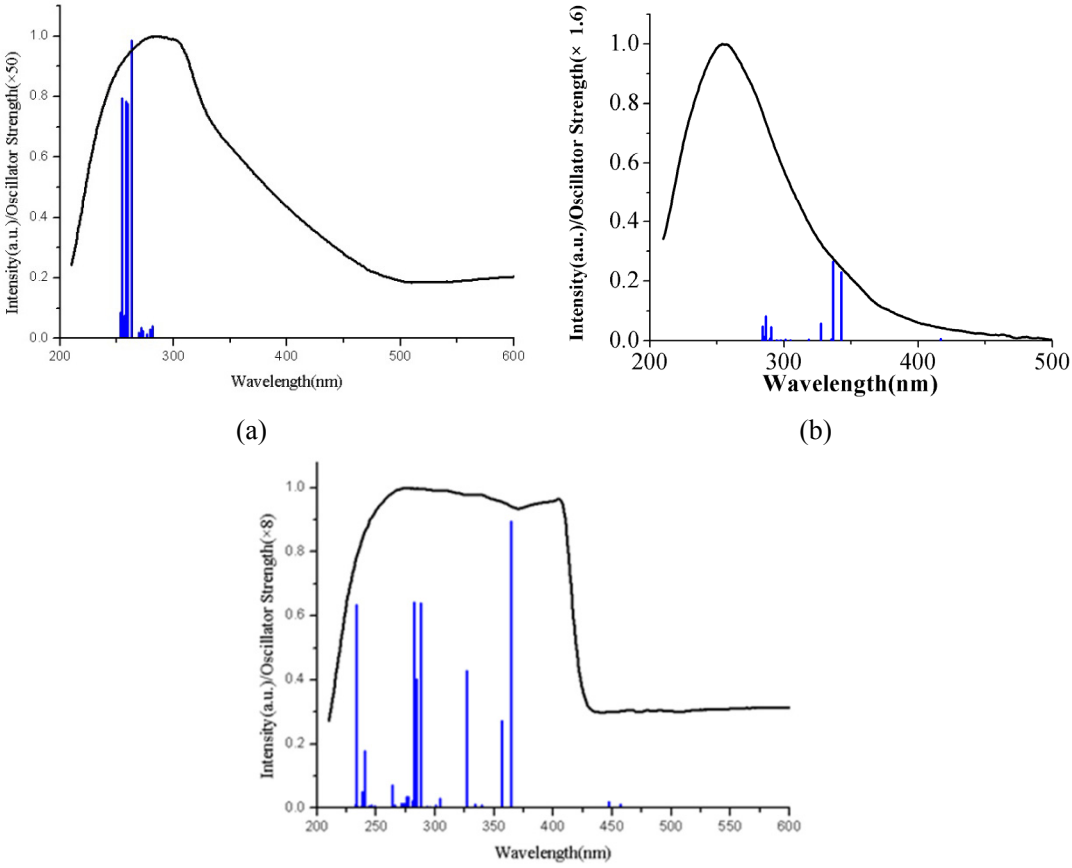

Fig. S17: Comparison of the experimental UV-vis absorption spectra (black curves) and the simulated ones (blue bars) of **1** (a), **2** (b) and **3** (c) at the TD-B3LYP level.

Additional spectral data:

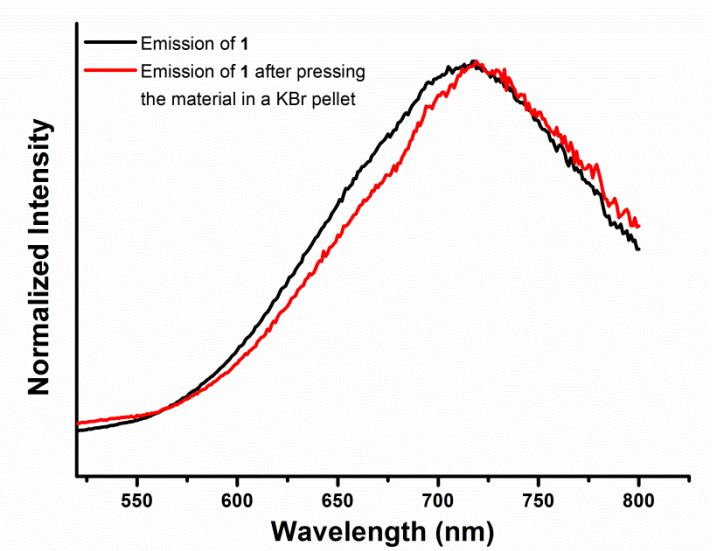

Fig. S18: Preliminary examination of the pressure effect by pressing the sample of **1** in a KBr pallet. It is found that the emission is sensitive to pressure, showing a slight red shift of the emission peak, which is attributed to the change in the Cu–Cu distance.

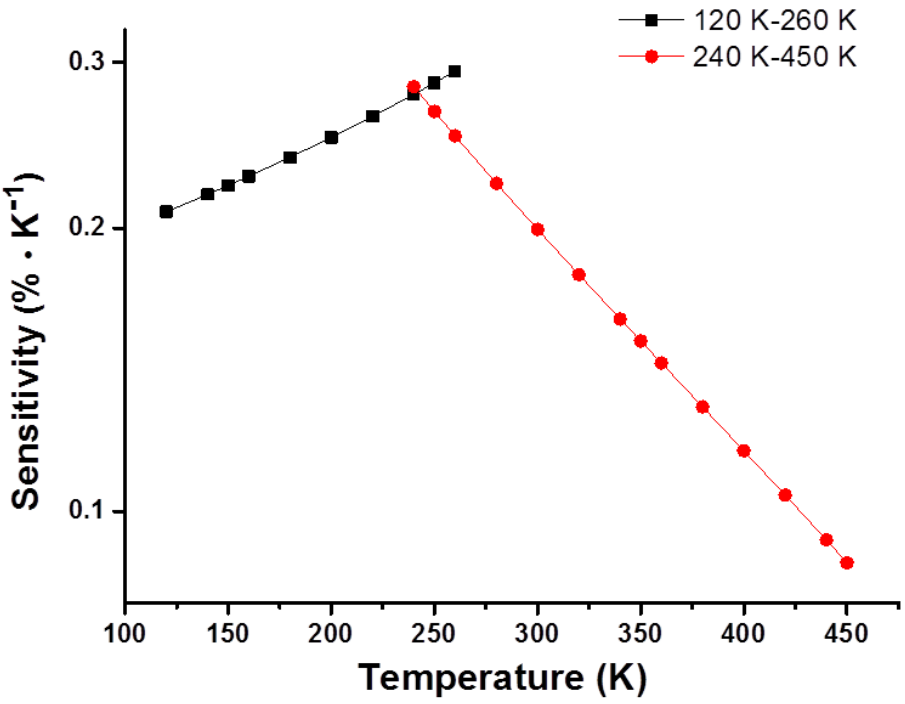

Fig. S19: Plots of relative sensitivity (calculated by the method reported by Carlos et al.[22]) of the luminescent molecular thermometer **2** in the range of 120–260 K and 240–450 K, respectively.

[22] A. Cadiau, C. D. S. Brites, P. M. F. J. Costa, R. A. S. Ferreira, J. Rocha, L. D. Carlos, *ACS Nano*, 2013, **7**, 7213.